

DESIGN AND FABRICATION OF NANOCHANNEL DEVICES

A Dissertation

by

MIAO WANG

Submitted to the Office of Graduate Studies of  
Texas A&M University  
in partial fulfillment of the requirements for the degree of

DOCTOR OF PHILOSOPHY

August 2009

Major Subject: Electrical Engineering

DESIGN AND FABRICATION OF NANOCHANNEL DEVICES

A Dissertation

by

MIAO WANG

Submitted to the Office of Graduate Studies of  
Texas A&M University  
in partial fulfillment of the requirements for the degree of

DOCTOR OF PHILOSOPHY

Approved by:

Chair of Committee,  
Committee Members,

Head of Department,

Jun Kameoka  
Chin B. Su  
Gerard L. Coté  
Robert D. Nevels  
Dimitris C. Lagoudas  
Costas Georghiades

August 2009

Major Subject: Electrical Engineering

## ABSTRACT

Design and Fabrication of Nanochannel Devices. (August 2009)

Miao Wang, B.En., University of Science & Technology of China

Chair of Advisory Committee: Dr. Jun Kameoka

Nanochannel devices have been explored over the years with wide applications in bio/chemical analysis. With a dimension comparable to many bio-samples, such as proteins, viruses and DNA, nanochannels can be used as a platform to manipulate and detect such analytes with unique advantages. As a prerequisite to the development of nanochannel devices, various nanofabrication techniques have been investigated by many researchers for decades. In this dissertation, three different fabrication approaches for nanochannels are discussed, including a novel scanning coaxial electrospinning process, a heat-induced stretching approach and a standard contact photolithography process. The scanning coaxial electrospinning process is established based on conventional electrospinning process. A coaxial jet, with the motor oil as the core and spin-on-glass-coating/PVP solution as the shell, is deposited on the rotating collector as oriented coaxial nanofibers. These nanofibers are then annealed to eliminate the core material and form the hollow interior. Silica nanochannels with an inner diameter as small as 15 nm were obtained. The heat-induced stretching approach includes using

commercially available fused silica tubings to create nanochannels by thermal deforming. This method and the electrospinning technique both focus on fabricate one-dimensional nanochannels with a circular opening. Fluorescent dye was used as a testing sample for single molecule detection and electrokinetic analysis in the resultant nanochannels.

Another nanochannel device described in this dissertation has a deep-shallow step structure. It was fabricated by standard contact lithography, followed by etching and bonding. This device was applied as a powerful detection platform for surface-enhanced Raman spectroscopy (SERS). The experiment results proved that it is able to highly improve the sensitivity and efficiency of SERS. The SERS enhancement factor obtained from the device is  $10^8$ . Moreover, the molecule enrichment effect of this device provides an extra  $10^5$  enhancement. The detection can be efficiently finished within minutes after simply loading the mixture of analytes solution and gold nanoparticles in the device. The sample consumption is in micro-liter range. Potential applications in diagnostics, prognostics and water pollutants detection could be achieved using this device.

## DEDICATION

*This dissertation is lovingly dedicated to my mother, Xianhuan Wang, for her support, sacrifice and love throughout my life.*

## ACKNOWLEDGEMENTS

I would like to thank my Ph.D. supervisor, Dr. Jun Kameoka. Throughout my doctoral studies, he provided encouragement, sound advice, good guidance and lots of good ideas. I owe him lots of gratitude for making my research life enjoyable and rewarding. I also want to thank my committee members, Dr. Cote, Dr. Nevels, Dr. Su and Dr. Lagoudas, for their guidance and support throughout the course of the research.

I wish to express my warm and sincere gratitude to all my lab buddies in Dr. Kameoka's group and Melodie Benford in Optical Biosensing Laboratory, for their friendship and help. They made the lab a convivial place to work.

Special thanks go to the department staff for making my time at Texas A&M University a great experience. I also want to extend my gratitude to the staff at Microscopy Imaging Center (MIC) and Materials Characterization Facility (MCF) at Texas A&M University and Cornell Nanofabrication Facility, who provided numerous helpful advice and suggestions during my experiments.

Lastly, and most importantly, I wish to thank my family for providing a loving environment for me. They are always the source of courage and inspiration.

## NOMENCLATURE

RT	Room Temperature
SOG	Spin-on-Glass Coating
AD	Alzheimer's Disease
A $\beta$	Beta Amyloid
BSA	Bovine Serum Albumin
HF	Hydrofluoric
SERS	Surface-enhanced Raman Scattering: SERS
A-Si	Amorphous Silicon
PECVD	Plasma-enhanced Chemical Vapor Deposition
CF <sub>4</sub>	Tetrafluoride

## TABLE OF CONTENTS

	Page
ABSTRACT .....	iii
DEDICATION .....	v
ACKNOWLEDGEMENTS .....	vi
NOMENCLATURE .....	vii
TABLE OF CONTENTS .....	viii
LIST OF FIGURES .....	x
LIST OF TABLES .....	xiv
1. INTRODUCTION: NANOCHANNELS AND THEIR APPLICATIONS .....	1
1.1 The Development of Nanochannel Devices .....	1
1.2 Overview of Fabrication Techniques .....	2
1.3 Importance of Research .....	5
2. NANOCHANNEL DEVICE FOR SINGLE MOLECULE DETECTION .....	7
2.1 Introduction .....	7
2.2 Background of Fabrication Technique: Basics of Electrospinning .....	9
2.3 Scanning Coaxial Electrospinning .....	15
2.4 Characterization of Electrospinning of Silica Nanochannel .....	19
2.5 Application: Single Molecule Detection .....	24
3. NANOCHANNEL DEVICE FOR ELECTROKINETIC ANALYSIS .....	28
3.1 Fabrication Technique: Heat-induced Stretching .....	28
3.2 Electrokinetic Analysis of Molecules in Nanochannel .....	32
4. NANOCHANNEL DEVICE FOR SURFACE-ENHANCED RAMAN SPECTROSCOPY .....	35
4.1 Introduction of Surface-enhanced Raman Spectroscopy .....	35
4.2 Mechanism of SERS .....	38
4.3 Overview of SERS-active Substrates .....	41



	Page
4.4 Design and Fabrication of Nanochannel Trapping Devices.....	50
4.5 Experiment Results.....	56
4.6 Application Examples.....	61
5. SUMMARY .....	75
REFERENCES.....	80
APPENDIX A .....	97
APPENDIX B .....	98
VITA .....	102

## LIST OF FIGURES

	Page
Fig. 1	Schematic diagram of a basic electrospinning setup. The inset shows a live image of an electrified Taylor cone and an extracted liquid jet.....10
Fig. 2	SEM images of nanofibers fabricated by electrospinning. (a) ZrO <sub>2</sub> nanofibers (b) SiO <sub>2</sub> nanofibers.....12
Fig. 3	(a) Schematic diagram of scanning electrospinning set-up (b) and (c) SEM images of aligned ZrO <sub>2</sub> nanofibers fabricated by scanning electrospinning.....14
Fig. 4	(a) Schematic diagram of coaxial electrospinning system (b) A double layered Taylor cone established on the needle tip.....17
Fig. 5	SEM images of electrospun silica nanochannels. (a) (b) Cross sections of silica nanochannels. These nanochannels were deposited on silicon wafer and cleaved to show the cross sections. (c) Top view of oriented parallel nanochannels. The scale bar is 100nm in (a) and (b), 10μm in (c).....19
Fig. 6	SEM and TEM images of incomplete nanochannel structures. (a)(c) SEM images (b) TEM image.....21
Fig. 7	SEM and TEM images of nanochannels. (a) SEM image of a broken nanochannel. (b) TEM image of a continuous nanochannel.....23
Fig. 8	The dimensions (O.D. and I.D.) of nanochannels as the function of the deposition distance.....24
Fig. 9	Schematic setup for single molecule detection. An 800nm-pulsed laser (two-photon excitation) was focused at the center of nanochannel with a spot size of 300 nm. Fluorescent emission signals from IAF were monitored by an avalanche photodiode (APD) and analyzed by computer. The nanochannel size and sample concentration defines the number of molecules passing through detection volume.....25

Fig. 10	<p>(a) Fluorescent optical micrograph of aligned nanochannel filled with IAF. The scale bar is 10 <math>\mu\text{m}</math>.</p> <p>(b) Schematic diagram of single molecule detection.</p> <p>(c) Photon counts of a blank nanochannel.</p> <p>(d) Photon counts of a nanochannel filled with a 4.9 <math>\mu\text{M}</math> of solution.....</p>	27
Fig. 11	<p>Schematic diagram of a prototype for heat-induced stretching method. The two ends of fused silica tubing are fixed on stage 1 and stage 2, respectively. Stage 1 is fixed and Stage 2 can be shifted horizontally to x-direction by rotating the handle. Butane torch is placed under the tubing to heat it up. The inset shows the deformation of the tubing under the heat and stretching. ....</p>	29
Fig. 12	<p>SEM images of stretched fused silica nanochannels with different shifts of (a) 1cm (b) 2cm (c) 3cm (d) 5cm.....</p>	30
Fig. 13	<p>Fluorescent image of IAF-filled fused silica nanochannel. Fluorescent dyes were drawn into the hollow channel by capillary force. The bright line is the filled channel.....</p>	31
Fig. 14	<p>Schematic diagram of experiment setup for electrokinetic effect in a nanochannel. A hollow nanochannel was deposited on quartz wafer, with two plastic reservoirs attached at two opening ends, respectively. After the channel was fully loaded with sample solution, an external electric field was applied through two electrodes immersed in two reservoirs to initiate the electrokinetic effect. An 800nm-pulsed laser source (two photon excitation) was focused at the center of the channel to excite the fluorophores. Emitted photons were collected by an avalanched diode.....</p>	32
Fig. 15	<p>Photon burst signal monitored over time in a nanochannel under different voltages. Emitted fluorescent photons from IAF were collected by an avalanched diode as the external electric field was changed. The averaged counts are the total photon burst collected in 10 sec. X-axis demonstrates time in a unit of <math>\mu\text{s}</math>. Y axis shows the number of collected photon counts. From the variance of photon counts under different voltage, the motion of fluorescent molecules in the channel can be analyzed.....</p>	33

Fig. 16	Averaged photon counts versus applied voltage. The dots in the graph demonstrate averaged counts under different voltage. The diffusion transport range is from 0 volts ~ 200volts, where no much difference was found in the number of averaged photon counts. In the electrokinetic transport range, a straight line is averaged between the lowest voltage (200 volts) and the highest voltage (600 volts). The detected counts at other voltages are evenly distributed along the line.....	34
Fig. 17	Schematic diagram of different processes.....	36
Fig. 18	Process flow chart of the fabrication process of nanochannel device....	52
Fig. 19	(a) Schematic diagram of a nanochannel device (side view) (b) Schematic diagram of a nanochannel device (top view) (c) SEM image of nanochannel cross section (d) SEM image of a nanochannel device (top view).....	53
Fig. 20	(a)(b) Optical microscopic images: aggregation of Au nanoparticles monitored over time (c) SEM image of gold nanoparticles aggregation at the boundary of microchannel and nanochannel (top view) (d) SEM image of gold nanoparticles in microchannel (top view) (e) SEM image of nanochannel area (top view).....	54
Fig. 21	Fluorescent image of polystyrene nanoparticles trapped at the step boundary of the nanochannel device.....	55
Fig. 22	SERS signals of adenine molecule obtained by different techniques (A) Raman signal without SERS active clusters, (B) SERS active clusters made by the conventional chemical method, (C) SERS active clusters created in a nanochannel device.....	56
Fig. 23	(a) SERS signal from 10 pM adenine collected at different time after the loading of the sample. (b) SERS signal from 10 pM adenine and 50 nM adenine monitored as a function of time.....	59
Fig. 24	(a) SERS spectra of 83nM adenine and 83 $\mu$ M congo red monitored in a nanochannel device over time (b) Magnified SERS spectrum detected using conventional SERS technique.....	61

	Page
Fig. 25	SERS spectra of A $\beta$ after 24 hours in the nanochannel device. (A) 11.5pM (B) 1.15nM (C) 11.5Nm.....64
Fig. 26	SERS spectra of soluble A $\beta$ (1.15nM kept at 6 °C) after (A) 48 hours and (B) 38 hours in the nanochannel device. Insoluble A $\beta$ oligomer (1.15 nM at room temperature) after (C) 48 hours and (D) 38 hours.....65
Fig. 27	SERS spectra of BSA at different temperatures (RT, 60°C, 100°C).....68
Fig. 28	SERS spectra of insulin at different temperatures (RT, 60°C, 100°C).....71

## LIST OF TABLES

	Page
Table 1 Assignment of peaks in BSA spectrum (RT).....	69
Table 2 Assignment of peaks in insulin spectrum (RT).....	71

## 1. INTRODUCTION: NANOCHANNELS AND THEIR APPLICATIONS\*

### 1.1 The Development of Nanochannel Devices

Since the discovery of lithography-based technology in 1950s, the miniaturization has made a significant change in our everyday life. From microelectronic chips to microelectromechanical systems (MEMS), smaller devices and higher integrations have been expected and actually realized at a fast pace. In 1990s, a research interest in fluid handling microchannel devices boosted because of their genomics application and potential capability in bio/chemical agent detection. Now the fabrication techniques have pushed those devices down to nanometer scale on which many fundamental biology processes occur, for example, information storage, transcription, translation, gene regulation, mitosis, and cell communication. Miniaturized assemblies can be designed to perform a wide range of tasks that range from detecting airborne toxins to analyzing DNA and protein sequences. Nanochannel devices have been widely explored as an experimental platform for direct manipulation and detection of bio-entities, such as DNA analysis,<sup>1,2</sup> cell handling, diagnostics,<sup>2</sup> protein analysis<sup>2</sup> and fluorescence correlation spectroscopy.<sup>3</sup>

---

This dissertation follows the style of *Lab on a Chip*.

\* Part of this section is reprinted with permission from *Nanofluidics*, Chapter 5 by Miao Wang and Jun Kameoka (Edited by Joshua B. Edel and Andrew J. deMello), 2009, RSC Publishing, UK, Copyright 2008 by The Royal Society of Chemistry. (<http://www.rsc.org/shop/books/2008/9780854041473.asp>)

By spatially confining target molecules within an ultra-small detection volume, nanochannel serves as a reliable and powerful analysis platform. The practical application of such a technology is highly dependent on the development of innovative fabrication techniques that can be used to create trenches on the nanometer scale. Although various microfabrication techniques have been developed and matured over the last 50 years,<sup>4</sup> nanofabrication method development is a more nascent research field and is currently being explored by many researchers. The vast majority of these researches are focused on how the resolution limitations of conventional micromachining methods may be overcome, whilst reducing fabrication cost and increasing throughput.

## 1.2 Overview of Fabrication Techniques

Nanochannel fabrication techniques can be broadly divided into two categories: top-down and bottom-up methods<sup>5</sup>. Top-down approach seeks to create nanoscale devices by using larger, externally-controlled ones to direct their assembly. Bottom-up approach seeks to have smaller components arrange themselves into more complex assemblies.

Lithographic processes including both light and electron beam methods define the standard top-down approach. These are widely used for device manufacture in the semiconductor industries. Within this general approach, a nanochannel may be defined using lithography, followed by reactive ion etching and then sealing or bonding of the structured substrate to a cover.<sup>6</sup> The ‘nano’ aspect of the channel or conduit is



lithographically defined during the resist patterning process. Unfortunately, this approach normally demands the use of high resolution lithography techniques, such as X-ray lithography,<sup>7</sup> e-beam lithography,<sup>8,9</sup> and proton beam lithography.<sup>10</sup> All such techniques can overcome the diffraction limit of light and thus improve feature resolution. However, the cost of ownership and system maintenance is extremely high. E-beam and proton beam lithography allows flexible pattern generation within a photoresist by using a 'mask-less' direct beam writing process. However the serial nature of this process also causes low throughput and thus makes it unsuitable for mass manufacturing. Focused-ion-beam milling<sup>11,12</sup> is another kind of direct writing process which rasters over and directly patterns a material. Needless to say, the process is not high-throughput in nature and is costly. Other lithographic techniques such as interferometric lithography<sup>13</sup> and nanoimprint lithography<sup>14,15</sup> have been assessed as tools for fabricating nanochannels in high-throughput. Interferometric lithography uses a standing wave pattern generated by multiple coherent optical beams to expose a photoresist layer. One of the primary challenges when using this approach is realizing pattern flexibility, since two-beam interferometric lithography will only produce periodic lines and spaces. Multiple beams and multiple exposures are currently being explored to create more complex structures.<sup>16,17</sup> Nanoimprint lithography is a simple process which transfers a pattern from a template to an imprint resist by mechanical deformation. Its utility depends on the structure of template, which is usually fabricated using ion beam lithography or electron beam lithography.

In addition to lithographic processing, an etching step is required to transfer the lithographically patterned nano-scale channel on the resist into a substrate such as fused silica or silicon. In this step, a channel depth in the nanometer range can be established. For instance, reactive ion etching can be controlled to produce a nanochannel with a sub-100nm depth on the surface of borosilicate<sup>18</sup> and silicon.<sup>19</sup> Wet anisotropic etching has also been used to develop nanochannels as shallow as 50nm on <110> silicon wafer using native oxide as the mask and Olin OPD 4262 positive resist developer as the etchant.<sup>6</sup>

The last step in top-down fabrication of a nanochannel is sealing or bonding. This process is used to enclose the etched trenches. There are a variety of ways to achieve a seal such as anodic bonding, fusion bonding, polymer bonding and eutectic bonding.<sup>5</sup> The selection of a sealing or bonding method depends sensitively on the substrate material being used. In addition, some sealing methods can narrow down the channel size. For example, Austin and co-workers reported the sealing of a nanochannel array generated by nanoimprint lithography by depositing SiO<sub>2</sub> over the trenches at a wide distribution of angles to create a capping layer. The local shadowing effects inherent in the deposition process reduced the cross section to approximately 10 nm<sup>14</sup>.

Self-sealed nanochannels have been fabricated by many researchers. For instance, sacrificial layer methods have been commonly used.<sup>9,20</sup> This approach involves patterning sacrificial materials on the surface of a substrate using high resolution patterning techniques such as e-beam or nanoimprint lithography. Subsequently a capping layer is deposited to cover the patterned sacrificial structure. In the final step, the

sacrificial layer is removed using chemical solvents or thermal decomposition. By using this approach, nanochannels with uniform height can be produced. However the removal of sacrificial material normally occurs over an extended time period, with conduit dimensions being sensitive to the patterning techniques used.

In general, top-down nanochannel fabrication methods are normally costly and generate rectangular or triangular shape cross-sectional profiles. Interestingly, reports relating to the bottom-up fabrication of nanochannels are much rarer, due to the difficulty in controlling the self-assembly process. In this process, atoms and molecules are initiated to arrange themselves into more complex nanostructure. Bottom-up approaches to nanochannel formation are however attractive due to their low cost and ability to create nanostructures with extremely small dimensions. Electrospinning, which is a simple and viable technique to fabricate continuous micro/nanofibers directly from a polymer/polymer-blended solution, is a classical self-assembly process. However opinions are split about whether electrospinning is a top-down or bottom-up fabrication method.<sup>21,22</sup> Details concerning this technique are discussed in section 2.

### 1.3 Importance of Research

In general, nanochannel devices can offer a number of advantages over conventional systems. (1) Extremely low sample consumption. Because of the low internal channel volumes, the consumption of fluid sample in nanochannel devices is usually in microliter or even smaller range. This is beneficial for applications with expensive or mass-limited sample; (2) Lab-on-a chip capability and faster operation.

Nanochannel devices of different functionalities can be integrated on one single chip. In this way, the sample preparation, reaction and waste collection can be finished sequentially. Higher analysis and control speed and better efficiency can be achieved due to short mixing times and fast heating. (3) Improved signal-to-noise ratio and sensitivity. (4) Cost-effective disposable chips can be fabricated in mass production.

With all of these advantages, nanochannels as a powerful detection platform were investigated. In this dissertation, different robust, low cost and reproducible fabrication techniques for nanochannel are demonstrated. These nanochannel devices have been applied to single molecule detection, electrokinetic analysis and ultra-sensitive characteristic molecule detection using surface-enhance Raman spectroscopy.

## 2. NANOCHANNEL DEVICE FOR SINGLE MOLECULE DETECTION\*

### 2.1 Introduction

Nanochannel systems have gained increasing attention in recent years because their representative small dimensions are comparable to the size of biomolecules such as proteins and DNA. Accordingly, they are expected to provide new ways to manipulate or detect such molecules with unrivalled precision. For instance, they have been used in DNA analysis<sup>23</sup>, single molecule detection<sup>24,25</sup> and fluorescence correlation spectroscopy.<sup>24</sup> Fluorescence spectroscopy has been used as a powerful tool for detecting molecules in a variety of chemical and biological systems for many years.<sup>26</sup> Fluorescence signals from specific fluorophores can be recorded and spectral, intensity, lifetime or polarisation information resulting can be used for molecular detection or identification. For the detection of single molecules in nanochannel, photon burst signals from single molecules traversing a sub-femtoliter optical probe volume can be used with auto-correlation or cross-correlation analysis for both molecule sizing and identification. Indeed, by fitting such correlation curves to theoretical models, much information relating to chemical kinetics and molecular mobility may be obtained. This so-called fluorescence correlation spectroscopy (FCS) is the most common method for detecting

---

\* Part of this section is reprinted with permission from *Nanofluidics*, Chapter 5 by Miao Wang and Jun Kameoka (Edited by Joshua B. Edel and Andrew J. deMello), 2009, RSC Publishing, UK, Copyright 2008 by The Royal Society of Chemistry.  
(<http://www.rsc.org/shop/books/2008/9780854041473.asp>)

Part of this section is reprinted with permission from “Electrospinning of Silica Nanochannels for single molecule detection” by Miao Wang, Nan Jing, Chin.B. Su et al., 2006. *Applied Physics Letters*, 88, 033106, Copyright 2006 by American Institute of Physics.

single molecules in liquid phase environments.<sup>27-50</sup> Nevertheless, conventional FCS methods normally generate information representative of all molecules passing through a given detection volume, and do not provide information about individual molecule. In recent years, FCS-based techniques have been used in conjunction with microchannels.<sup>51,52</sup> Laser light is focused in the centre of a microchannel, and the fluorescence signals originating from individual molecules passing through this probe volume are detected by an avalanche photodiode. Compared to conventional FCS, the incorporation of a microchannel system for sample manipulation has several advantages. First, the statistical accuracy of single-molecule characterization is improved because all (or the vast majority of) molecules are counted and contribute to the statistical analysis. In addition, detection throughput can be controlled in a facile manner. The number of molecules detected per unit time can simply be increased by increasing the electrical potential or flow pumping speed. Significantly, this control can be used to drastically reduce the assay time. Moreover, because of the small detection volume, the signal-to-noise (S/N) ratio is improved.<sup>53-58</sup> To further improve the S/N ratio, nanochannels can be utilized for single molecule detection since they act to decrease the size of detection probe volume. A reduced detection volume will significantly improve the S/N ratio and decrease the probability of multiple molecule occupancy of the detection volume. For instance, the S/N ratio obtainable in 800 nm square-shaped channels is 5 times better than 20  $\mu\text{m}$  square-shaped channels. This is why nanochannel is more powerful in single molecule detection comparing to microchannel or even larger scale devices.

As discussed in previous section, there are many top-down processes to fabricate nanochannel. However, these processes are usually expensive and time consuming. In addition, it is difficult to create circular nanochannels with a size less than 50 nm which are beneficial for single molecule diagnostics. We have designed a novel “scanning coaxial electrospinning” process, which has turned out to be a successful bottom-up approach to fabricate nanochannel. Previously, hollow nanofibers were fabricated by the coaxial electrospinning.<sup>59,60</sup> In this process, a two-capillary coaxial nozzle was designed to form the coaxial source required to generate the precursor of hollow nanofibers. But the resulting randomly deposited hollow nanofibers are not suitable for molecule diagnostics or to be integrated in a complex nanochannel chip. By constructing a unique electrospinning set-up, our approach is able to fabricate parallel oriented nanochannel as small as 15 nm with a circular/oval cross section efficiently and cost-effectively.

## 2.2 Background of Fabrication Technique: Basics of Electrospinning

In 1934, Anton Formhals invented a spinning technology that produced synthetic fibers with the aid of an electric field.<sup>61</sup> This invention did not gain widespread attention until the 1990s when researchers demonstrated its capacity to produce nanoscale polymer fibers.<sup>62</sup>

A typical electrospinning process involves the extrusion of a polymer solution from a needle or spinneret by applying a high voltage. A so-called “Taylor cone” is formed at the tip of the spinneret since the induced charges in the polymer solution are attracted by the electrostatic force. A grounded collector or a counter electrode is placed several centimeters away from the spinneret or source. When the applied voltage

exceeds a threshold value, a polymer jet is extruded because the electrostatic force overcomes the surface tension of polymer solution, and the polymer erupts from the Taylor cone and travels towards the grounded collector, which is a lower potential zone, under an electrostatic stretching force. In this procedure, the liquid jet experiences a bending and whipping motion due to charge repulsion between molecules incorporated in the liquid jet. The repulsion of electric charges in the jet continuously stretches and minimizes the diameter of the jet. In the meantime, the solvent evaporates and leads to size-shrinking and solidified micro/nanofibers on the grounded collector. A piece of aluminium foil or a silicon wafer may be attached to the collector for collecting nanofibers. A schematic diagram of a basic electrospinning process is shown in Fig. 1.

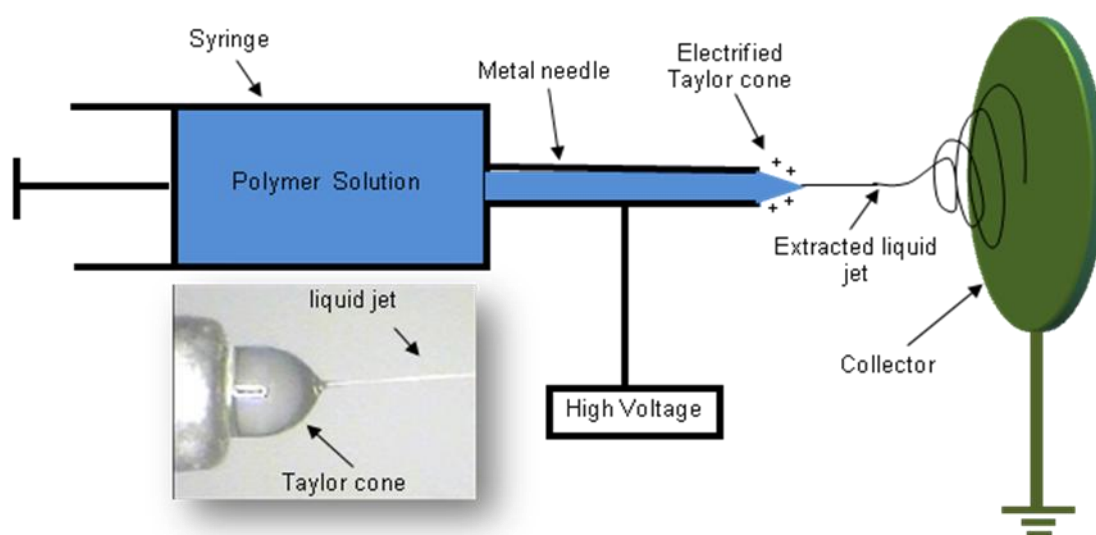


Fig. 1 Schematic diagram of a basic electrospinning setup. The inset shows a live image of an electrified Taylor cone and an extracted liquid jet.



Nanofibers with a solid interior and a smooth surface can be fabricated by a normal electrospinning process. An appropriate polymer solution is a prerequisite for this technique. Electrospinning is able to produce long, thin and continuous fibers from various materials including polymers, ceramics and composites. A broad range of polymers have been directly electrospun into nanofiber format, including polyvinyl pyrrolidone (PVP),<sup>62</sup> poly(vinylidene fluoride) (PVDF),<sup>63,64</sup> poly(caprolactone),<sup>65,66</sup> poly(glycolide) (PGA),<sup>67</sup> poly(L-lactide) (PLA),<sup>67</sup> polystyrene (PS),<sup>68</sup> polyethylene oxide (PEO),<sup>66</sup> polyvinyl alcohol (PVA), etc.<sup>66</sup> Because of the simplicity and low-cost of electrospinning, much effort has been focused on expanding the scope of “electrospunable” materials and associated applications.

By blending sol-gel precursors with polymers such as PVP, PVA and PEO, metal oxide nanofibers, ceramic nanofibers and even non-metal-oxide ceramic fibers can be produced effectively.<sup>62</sup> Fig. 2 shows examples of ZrO<sub>2</sub> and SiO<sub>2</sub> nanofibers fabricated by electrospinning. Carbon nanotubes, nanoparticles, drugs, dyes, enzymes and DNA have also been incorporated into nanofibers successfully. The large surface area-to-volume ratio is especially favorable for many applications such as biomedical scaffolds in tissue engineering, chemical catalysts, or sensors.<sup>62</sup>

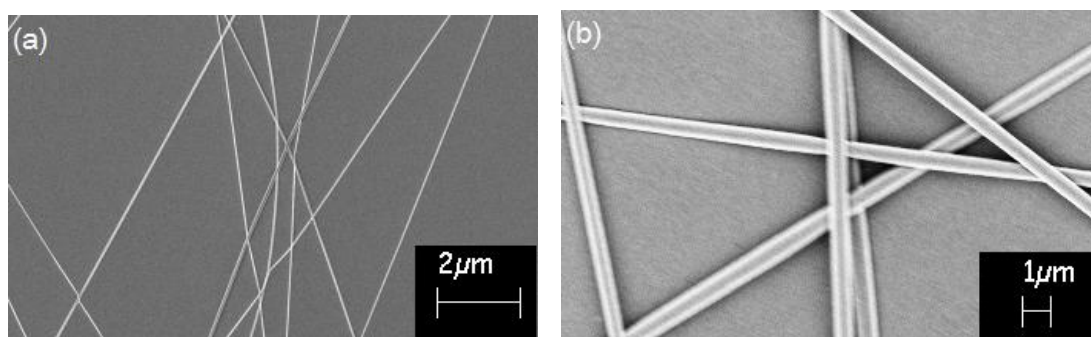


Fig. 2 SEM images of nanofibers fabricated by electrospinning. (a)  $\text{ZrO}_2$  nanofibers (b)  $\text{SiO}_2$  nanofibers.

Various factors can influence the electrospinning process. The primary processing parameters involve: (1) The properties of polymer solution (e.g. viscosity, electrical conductivity and surface tension). The viscosity can be controlled by varying the polymer type and concentration. Different solvents and additives can be used to control the electrical conductivity and surface tension of the solution. (2) The applied voltage, which affects the electric field between the nozzle and the collector, can be adjusted using an external power supply. The applied voltage controls the extrusion force of the liquid jet, which must be balanced with the surface tension and viscous forces of the polymer solution. (3) The flow rate, which defines the rate that the electrospun polymer solution is supplied. This can be adjusted by a mechanical pump connected to a syringe, and controls the volume of solution emerging from the nozzle per unit time. (4) The deposition distance, which is the distance between the nozzle tip and the grounded collector. The magnitude of this distance affects the amount of solvent evaporated before any nanofibers are formed and deposited on the counter electrode. (5) Environment conditions, such as humidity and temperature. A stable electrospinning process can be established through consideration and optimization of all of the above

parameters. Post-treatment steps (for example calcination) are often employed after the collection of metal-oxide or ceramic nanofibers.<sup>22,69,70</sup> Such treatment can remove unnecessary polymer matrices in resultant fibers.

Usually, fibers are randomly distributed on the surface of the collector. In order to obtain aligned nanofibers, the basic electrospinning process must be modified. For example, pairs of split strips have been used to orient electrospun nanofibers.<sup>71,72</sup> In such a setup, the solid grounded collector is substituted by a pair of conductive substrates with a void gap or patterned gold-electrode pairs on highly insulating substrates. When a continuous fiber is deposited on the collector, the electrostatic interaction in as-spun fibers initiates alignment. Another aligned nanofiber collection technique has been developed by Zussman's group.<sup>73</sup> They demonstrated the effectiveness of using a tapered and grounded wheel-like rotating bobbin as the collector to obtain parallel nanofibers. Since the collector is not flat, the challenge when using this bobbin collector is to transfer nanofibers onto a planar surface for possible integration with other devices and applications. Additional rotating collectors have been proposed by Kameoka and co-workers to define "scanning electrospinning" techniques.<sup>74,75</sup> A schematic of the process is provided in Fig. 3(a). The grounded collector is connected to an electric rotational motor and rotates at high speed. A substrate is attached to the rotating collector where nanofibers will be deposited. Nanofibers can be deposited in an aligned fashion due to the rotation and relative motion between the electrospinning nozzle and the counter electrode. The orientation of nanofibers is controlled by the linear velocity of rotating collector. In this way, nanofibers can be aligned in a facile manner and collected on the

flat substrate for further treatment and applications. Fig. 3(b) and (c) show parallel-aligned  $\text{ZrO}_2$  nanofibers on silicon wafers.

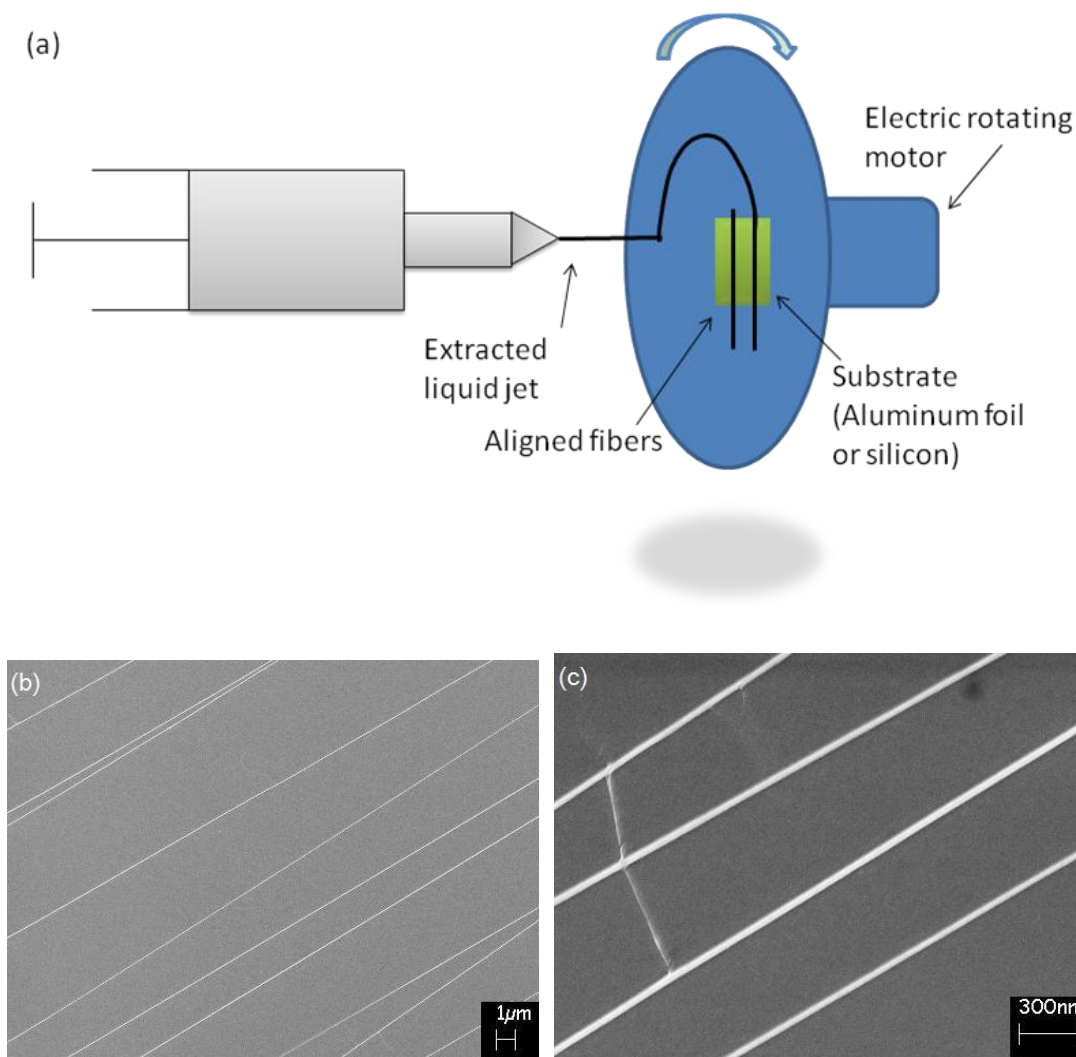


Fig. 3 (a) Schematic diagram of scanning electrospinning set-up (b) and (c) SEM images of aligned  $\text{ZrO}_2$  nanofibers fabricated by scanning electrospinning.

The basic electrospinning process has also been modified in a variety of ways to produce nanofibers with a range of secondary structures. For example, conjugated polymer nanofibers,<sup>76</sup> core-sheath nanofibers,<sup>77,78,79</sup> hollow nanofibers,<sup>59,80</sup> porous

nanofibers<sup>81</sup> have all been produced by coaxial electrospinning from a two-fluid capillary spinneret. Nanofibers conjugated with fluorescent probes,<sup>82</sup> metal oxide particles<sup>83</sup> and nanoparticles of noble metals<sup>84,85</sup> have been reported.

For more detailed information about the electrospinning process, there are some excellent review articles.<sup>21,22,62,86,87</sup> Theoretical analyses of the electrospinning process can also be found.<sup>88-91</sup> However, due to complex effects of diversified processing parameters, accurate modeling of electrospinning is still challenging. In the following sections, we will focus on the apparatus developed for coaxial electrospinning of silica nanochannel.

### 2.3 Scanning Coaxial Electrospinning

The fabrication of nanochannel by electrospinning has also been explored previously. Put simply, methods are divided into two categories. In the first, nanofibers are used as templates, and in the second nanochannel fabrication occurs directly. In the former, coating materials are deposited on the surface of deposited nanofibers. Then the nanofibers core is decomposed by heating or dissolution in an appropriate solvent to create the desired hollow structure. This method is conceptually similar to the fabrication of nanochannel by sacrificial layer methods discussed previously. The primary difference between these approaches lies in the generation of the sacrificial layer. Compared to other methods, electrospinning is more straightforward, economical and efficient. One of the key decisions made in this process is the choice of polymer to produce the nanofibers and shell materials. First of all, the polymer should be able to be

electrospun and produce nanofibers with reduced dimensions. It should also be stable during the deposition process and easily removable in the final process. The shell material needs to be robust enough to retain its morphology during the decomposition of core and construction of the wall of nanochannel. To date, polymer, metal, metal oxide, and ceramic nanotubes have been produced using this general method.<sup>92-96</sup>

The direct deposition method, which is typically called a coaxial electrospinning, defines the alternative approach for fabricating nanochannels. For example, a two-capillary spinneret has been used to generate nanochannel previously.<sup>59,80,81</sup> Moreover, a similar electrospinning deposition system was used to fabricate core-shell nanofibers.<sup>77-79</sup> By dispensing two immiscible materials (such as oil and water) in a coaxial spinneret, a coaxial jet can be extruded by electrostatic forces to create coaxial nanofibers. Subsequently, the core material can be removed by heating to create nanochannel.

To simplify the fabrication process, an innovative coaxial electrospinning system incorporating a scanning function was developed by the precise alignment of two independent metal needles. Significantly, this system can easily generate oriented nanochannels.<sup>97</sup> Instead of using two-capillary nozzles as the coaxial source, two needles are aligned in an “L” shape arrangement. Using such an alignment, a coaxial jet can be generated directly. A schematic of this deposition system is shown in Fig. 4(a).

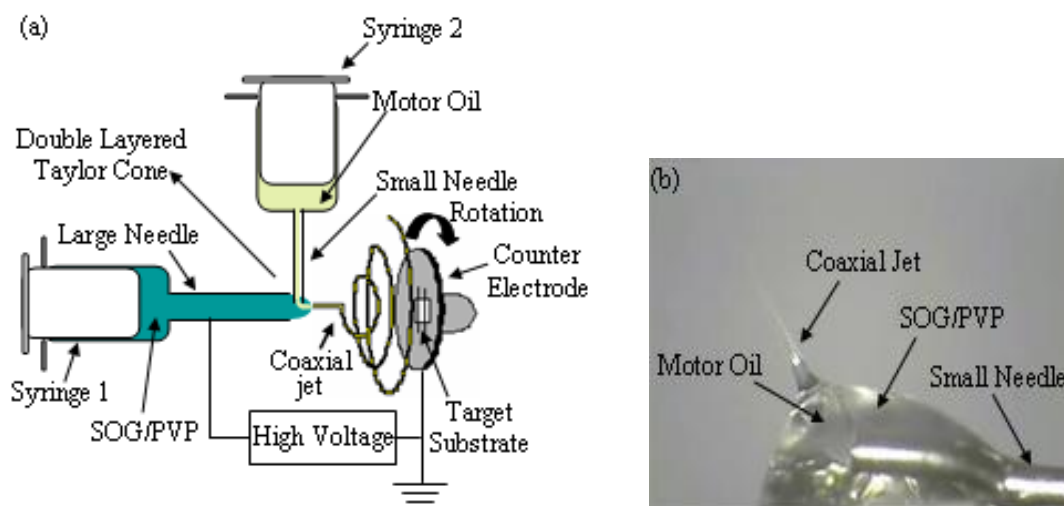


Fig. 4 (a) Schematic diagram of coaxial electrospinning system (b) A double layered Taylor cone established on the needle tip.

Two syringes, syringe pumps, needles and positioning stages were used for this scanning coaxial electrospinning system. One syringe is filled with the shell material. In our experiment, a blend of spin-on glass (SOG) intermediate coating IC1-200 solution and polyvinylpyrrolidone (PVP) (MW~1,300,000) was used as the shell material. SOG is a precursor for silica, which is common substrate material in biological applications due to its biocompatibility and stable chemical and physical properties. PVP acts to introduce an appropriate viscosity to the precursor solution, which is required to extract a continuous jet and establish a stable electrospinning process. In its native form PVP is a white, hygroscopic powder which can be readily dissolved both in deionised water and in a large number of organic solvents. The weight percentage of PVP in the whole solution varies from 4% to 8%. The mixture is stirred using a magnetic bar until the PVP is completely dissolved, resulting in a viscous and transparent solution.

The other syringe is infused with the core material, which is also the sacrificial material (SAE 10W30 motor oil), and connected to a small needle (33 Gauge, Hamilton). The SOG/PVP blend and motor oil are delivered at different rates by independent syringe pumps fixed on two positioning stages, and the anode of the power supply is connected to the large needle. By horizontal and vertical adjustment, the needle is precisely inserted in the Taylor cone of SOG/PVP stream. Due to their immiscibility, the core and shell phases do not inter-diffuse into each other and a double-layered Taylor cone is generated. The adjustment of needle position and the Taylor cone are monitored with a microscope. A live image of a core-shell Taylor cone is shown in Fig. 4(b). The coaxial jet is pulled out and transported to the counter electrode which is rotating at a high speed.

To produce oriented nanochannels, scanning electrospinning is implemented. A piece of silicon wafer is attached onto the rotating counter electrode. Aligned nanofibers with SOG/PVP as the wall and motor oil as the core are deposited. Then, the wafer is calcined within a furnace at 850°C for 5 hours to cross link the silica as well as completely remove residual PVP and motor oil. In this way, hollow structured nanofibers are obtained. SEM images in Fig. 5 confirm the effectiveness of this fabrication method. Nanochannels with a round/elliptical opening are shown in Fig. 5(a) and Fig. 5(b). A top view of the silicon wafer in Fig. 5(c) shows the nanochannels aligned in a parallel fashion.



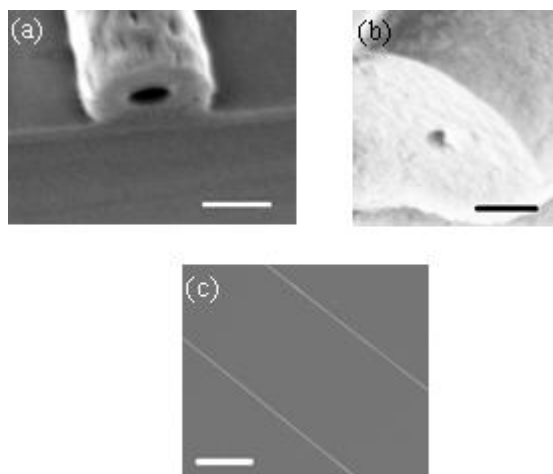


Fig. 5 SEM images of electrospun silica nanochannels. (a) (b) Cross sections of silica nanochannels. These nanochannels were deposited on silicon wafer and cleaved to show the cross sections. (c) Top view of oriented parallel nanochannels. The scale bar is 100nm in (a) and (b), 10 $\mu$ m in (c).

#### 2.4 Characterization of Electrospinning of Silica Nanochannel

When fabricating silica nanochannels, there are several process parameters that influence the channels' morphology. These include the needle alignment, the flow rates of the SOG/PVP and motor oil and the viscosity of shell material. A list of processing parameters in a successful scanning coaxial electrospinning process is included in Appendix A. Precise alignment of two needles is necessary to ensure a stable coaxial source. The motor oil must be fully surrounded by SOG/PVP, which also means that the flow rate of motor oil cannot be too high so as to disrupt the interfacial layer of oil-SOG/PVP. If this happens, oil will spread out from the wrapping of the outer solution and disturb the spinning process. However, the flow rate of the motor oil must be high enough to allow formation of a continuous core. Inappropriate process parameters will have a significant and deleterious impact on the final structure of the spun fibers. Fig. 6 illustrates the outcome of misalignment and improper flow conditions. Fig. 6(a)

describes a situation in which the oil-feeding needle tip is placed too close to the edge of SOG/PVP Taylor cone. Although the motor oil can be extruded together with SOG/PVP solution and enclosed, it cannot be confined perfectly and firmly in the outer layer during the stretching, bending and whipping processes. Instead of forming an inner sacrificial medium, some oil molecules diffuse to the outer layer of the SOG/PVP fiber. Because of this diffusion, subsequent to calcination, an unsealed trench is created. Fig. 6(b) shows a TEM image of discontinuous nanochannels. In this example, the supply of oil is insufficient to cover the stretching of SOG/PVP fibers under electrostatic force. Therefore, tubular segments of nanofibers are formed. Unenclosed nanofiber segments can also be seen along with a non-uniformity in nanofiber diameter (Fig. 6(c)). This is likely to be a result of both misalignment and inadequate flow rate.

The flow rate of the oil stream also has influence on the inner diameter of the channel. As the flow rate increases within a reasonable range, more core material is pumped out per unit time, resulting in a larger core and inner diameter. An oil flow rate between  $2\mu\text{l}/\text{min}$  and  $6\mu\text{l}/\text{min}$  defines an appropriate range for generating nano-scale silica channels for 5 wt% PVP in an SOG polymer solution with an average electric field of  $525\text{V}/\text{cm}$ . It should be noted that lower and higher flow rates may also work, but may require adjustment of other processing parameters, such as PVP concentration, electric field and needle size.

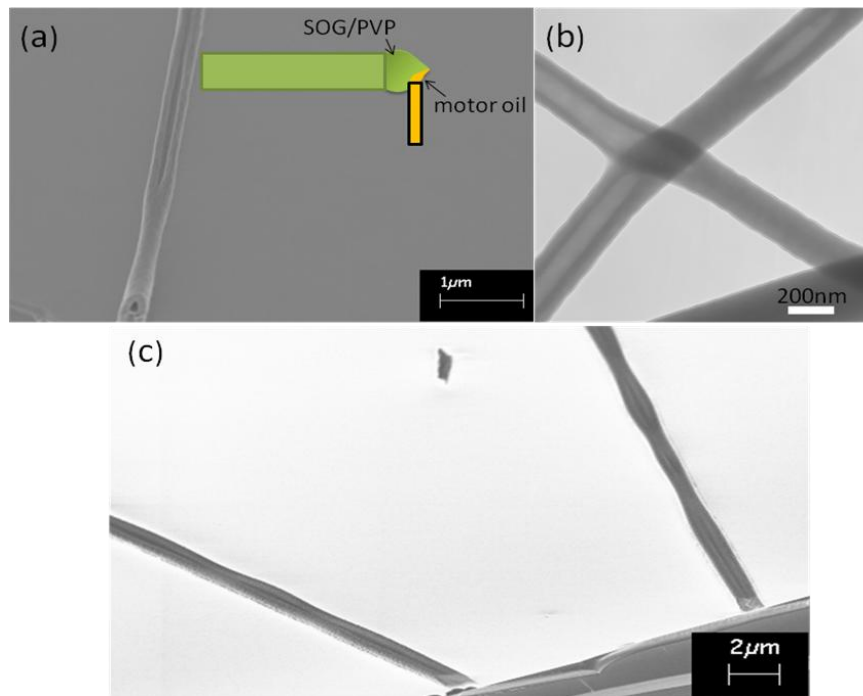


Fig. 6 SEM and TEM images of incomplete nanochannel structures. (a)(c) SEM images (b) TEM image.

The concentration of PVP has a direct influence on the viscosity of the polymer solution. A typical range of PVP concentration for the described experiments is between 4 wt. % and 8 wt. %. As the PVP concentration increases in the solution, a concomitant increase in viscous stress provides better confinement of the oil phase. Accordingly, the oil can be extruded into a thinner core, thus generating smaller diameter channels. The nanochannel shown in Fig. 5(a) has an average of 60nm and was fabricated with a 5 wt. % PVP in SOG solution. Conversely, the nanochannel shown in Fig. 5(b) has an average diameter of 15nm and was obtained from an 8 wt. % PVP in SOG solution.

As the concentration of PVP increases, the flow rate of motor oil must be increased accordingly to compensate for the increased viscous stress caused by the increased PVP concentration. By balancing all these process parameters, silica

nanochannels can be created successfully (Fig. 5(a) and (b)). From SEM image analysis, some broken nanochannels can be seen. One example is shown in Fig. 7(a). In this image, a round channel shape is clearly observed. This confirms that the oil is extruded out as the core and retains a cylindrical structure without collapsing in the electrospinning and calcination process. Through use of proper process parameters, continuous nanochannels can be created. A TEM image in Fig. 7(b) demonstrates such an example. The brighter part of this image illustrates the hollow interior with the darker region representing the wall.

Previous research on controlling the diameter of electrospun nanofibers, has suggested that the nanofiber diameter can be controlled by varying the deposition distance. This is because the transit time for the electrified jet increases correspondingly as the deposition distance increases. With a longer time in transit, more solvent evaporates and the diameter of nanofiber can be reduced. We have also studied how the deposition distance affects the dimensions of nanochannels. Fig. 8 illustrates the variation of the inner diameter (I.D.) and outer diameter (O.D) of nanochannels as a function of deposition distance. It indicates that no obvious change in I.D. and O.D. occurs when the deposition distance varies. This observation might be explained by the structure of coaxial liquid jets extruded during the electrospinning process. The motor oil cannot evaporate through the SOG/PVP wall layer. Thus, the shape of motor oil is maintained and the I.D. of the nanochannel will not vary. Additionally, the O.D of nanochannel shows no obvious dependence on the deposition distance in a range of 5.3cm to 15.3cm.

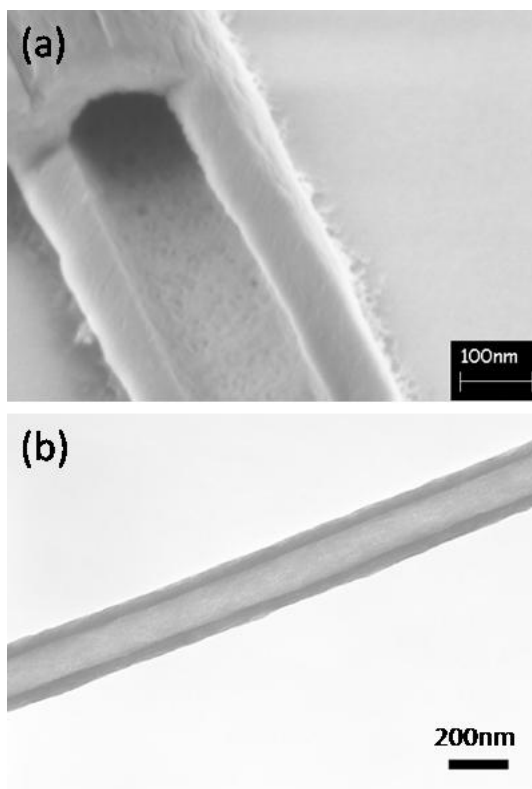


Fig. 7 SEM and TEM images of nanochannels. (a) SEM image of a broken nanochannel. (b) TEM image of a continuous nanochannel.

To control the orientation of the coaxial nanofibers, we have used the scanning technique to create parallel nanofibers. A rotating counter electrode with a linear velocity between 660 and 850 cm/s was placed at the collecting position, and a relative motion between the coaxial jet and target substrate (a silicon wafer attached to the counter electrode 4.5 cm away from the centre) was used. The orientation of nanofibers can be controlled via a linear scanning motion rather than the random spinning motion.<sup>74</sup> In conclusion, silica nanochannels can be fabricated using the scanning, coaxial electrospinning process. The instrumentation can be set up easily and involves the use of

two aligned syringes rather than specially designed spinnerets. By rotating the counter electrode and removing the core of the coaxial nanofibers, parallel oriented and circular silica nanochannels with an I.D. as small as 15 nm can be formed. Due to their extremely small dimensions, these nanochannels have many potential applications, especially in facilitating high-efficiency single molecule detection.

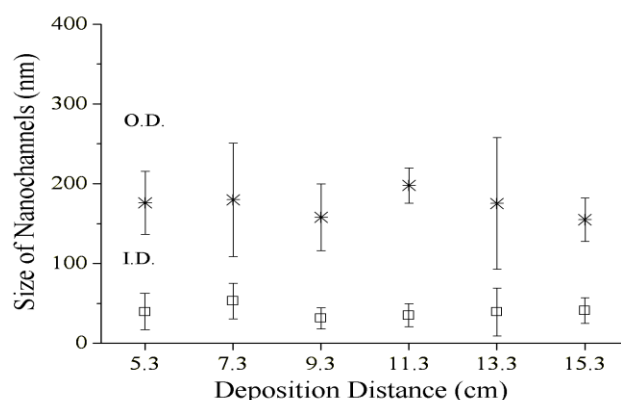


Fig. 8 The dimensions (O.D. and I.D.) of nanochannels as the function of the deposition distance.

## 2.5 Application: Single Molecule Detection

To investigate the performance of nanochannels for single molecule analysis, IAF was utilized as a sample solution. A schematic diagram of the detection system employed is illustrated in Fig. 9. The scanning coaxial electrospinning technique was used to fabricate silica nanochannels as previously described. A substrate is used to hold and align the electrospun nanochannels. The substrate needs to be both robust (in order to withstand the high-temperature calcination process) and also transparent to visible light (to allow efficient molecule excitation and fluorescence detection). Accordingly, a quartz wafer is commonly used to collect aligned electrospun nanochannels. Plastic

reservoirs can be attached at the both sides of nanochannels, and the sample solution injected into a reservoir and infused into the nanochannel using capillary force. For the experiments described herein an 800 nm laser with a pulse duration of 80 fs and a repetition rate of 80MHz was focused into the nanochannel. As fluorescent molecules pass through the detection volume, they are excited (via two-photon absorption) and emit fluorescence photons in the visible region of the electromagnetic spectrum. Fluorescence photons are collected and detected using an avalanche photodiode, and are then processed and displayed as photon burst counts per unit time.

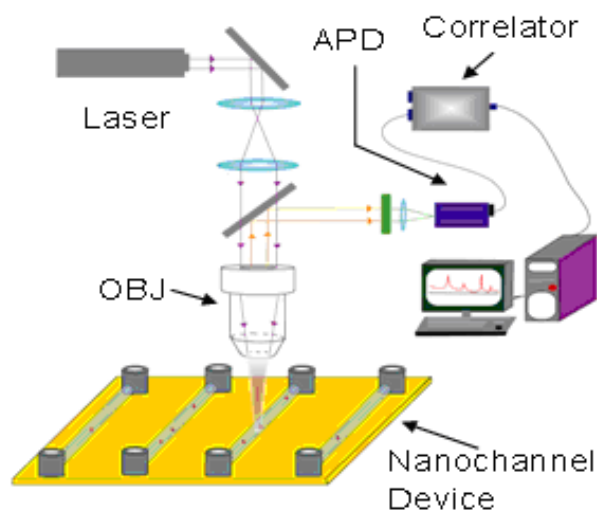


Fig. 9 Schematic setup for single molecule detection. An 800nm-pulsed laser (two-photon excitation) was focused at the center of nanochannel with a spot size of 300 nm. Fluorescent emission signals from IAF were monitored by an avalanche photodiode (APD) and analyzed by computer. The nanochannel size and sample concentration defines the number of molecules passing through detection volume.

Single molecule detection has been performed within electrospun channel having an inner diameter of 25 nm. A 4.9  $\mu\text{M}$  solution of IAF in EPPS buffer (pH=9) was infused into the nanochannels. Fig. 10(a) shows an image of aligned IAF filled

nanochannels. Channel integrity is confirmed through the observation of no dye leakage. Single molecule detection was then demonstrated within this nanochannel. Fig. 10(c) and (d) display the photon burst signals before and after filling the nanochannels with IAF molecules. The x-axis defines the time points at which data are acquired during analysis, with the Y-axis representing the number of photon counts per bin time. In simple terms, a sub-femtolitre probe volume is defined by the overlap between a focused laser beam and the nanochannel. As a single molecule diffuses through this volume it can be repeatedly cycled between its ground and excited states to yield a burst of fluorescence photons which can be collected and detected. Fig. 10(c) and (d) report photon counts every  $10\mu\text{s}$  bin within a 2ms time period. For an empty nanochannel, no photons are observed. After the injection of IAF molecules, photon burst peaks originating from single molecule events are detected. Based on the size of nanochannel and the size of the laser beam waist, the detection volume of this system was calculated to be 150 zeptoliters. With a  $4.9\mu\text{M}$  solution, the average number of molecules in the detection volume at any instant is approximately 0.4, which satisfies the single molecule standard. To put this context, for a microchannel with a  $1\mu\text{m}$  inner diameter, the average number of molecules in the detection volume for a  $4.9\mu\text{M}$  solution is approximately 695. This occupancy is clearly far from the requirements of single molecule detection! Indeed, for this microchannel environment, single molecule detection can only be achieved with a solution concentration of less than 7nM.



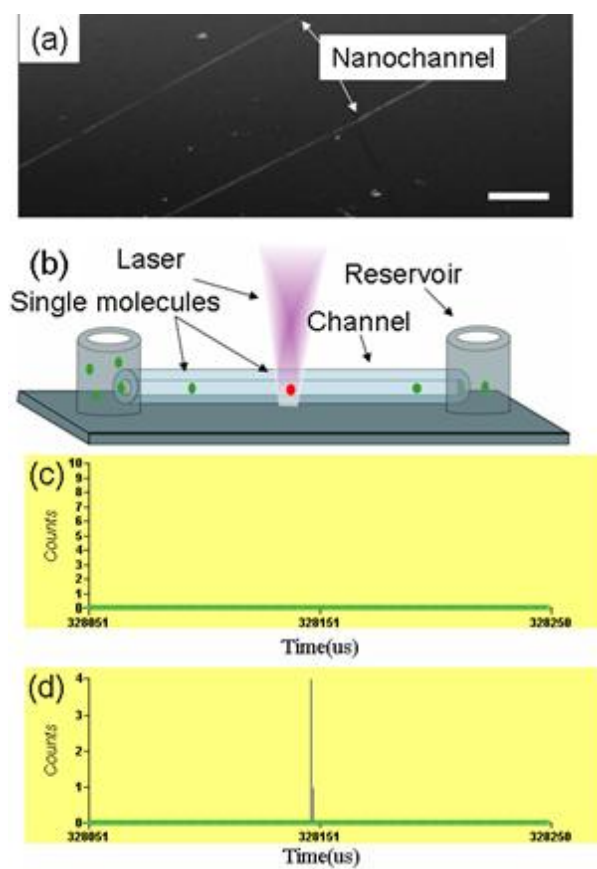


Fig. 10 (a) Fluorescent optical micrograph of aligned nanochannel filled with IAF. The scale bar is 10  $\mu\text{m}$ . (b) Schematic diagram of single molecule detection. (c) Photon counts of a blank nanochannel. (d) Photon counts of a nanochannel filled with a 4.9  $\mu\text{M}$  of IAF solution.

### 3. NANOCHANNEL DEVICE FOR ELECTROKINETIC ANALYSIS\*

#### 3.1 Fabrication Technique: Heat-induced Stretching

Due to the physical properties of silica, the thermal deformation of micro-silica tubes is another way to form nanoscale channels. Indeed, there is a long history of heat deformation of glass in industrial and artistic applications. Moreover, a detailed theoretical analysis of thermally-induced glass tube stretching for fabricating glass microelectrodes can be found elsewhere.<sup>98</sup> Non-silica based glass has also been shown to form holey fibers by thermally-induced drawing methods.<sup>99</sup> However, the fabrication of nanochannels by this approach has not been investigated in any detail. A prototype system for nanochannel fabrication is shown in Fig. 11. The primary parts of this system include two stages, a butane torch, capillary tubing with a 12 $\mu$ m thick coating of polyimide and a fused silica capillary cutter. Stage 1 is fixed onto the lab bench, and stage 2 can be mechanically moved. A void gap of  $\sim$ 1cm is created between the edges of the two stages. The ends of the capillaries are glued to the each of the two stages. A butane torch is then placed in the gap beneath the tubing. After the torch is ignited the polyimide coating can be rapidly eliminated in a defined area. Within a further few seconds, the fused silica is softened by heat. Stretching of glass tubing process is performed using Stage 2, which is shifted in the x-direction. The fused silica tubing gradually deforms, tapers and shrinks. The inset of Fig. 11 shows a magnified schematic diagram of a deformed part of the tubing under the application of heat.

---

\* Part of this section is reprinted with permission from *Nanofluidics*, Chapter 5 by Miao Wang and Jun Kameoka (Edited by Joshua B. Edel and Andrew J. deMello), 2009, RSC Publishing, UK, Copyright 2008 by The Royal Society of Chemistry. (<http://www.rsc.org/shop/books/2008/9780854041473.asp>)

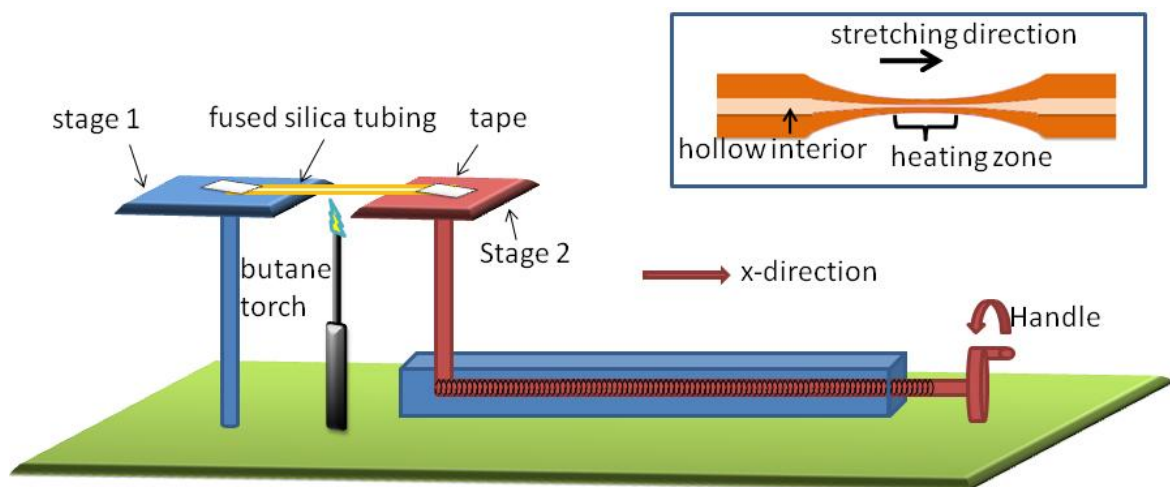


Fig. 11 Schematic diagram of a prototype for heat-induced stretching method. The two ends of fused silica tubing are fixed on stage 1 and stage 2, respectively. Stage 1 is fixed and Stage 2 can be shifted horizontally to x-direction by rotating the handle. Butane torch is placed under the tubing to heat it up. The inset shows the deformation of the tubing under the heat and stretching.

The shift distance of Stage 2 has a significant effect on the size of final nanochannel. The final channel may be cut with a razor blade in the centre to show the cross section. Fig. 12(a)-(d) show the cross section of stretched fused silica tubes with a shift of 1cm, 2cm, 3cm and 5cm respectively. With a 1cm shift, the inner diameter of silica tubing is reduced to  $\sim 250$  nm. For longer shift distances, e.g. 5cm, the inner diameter is reduced but finally collapses under heating and results in a solid segment of fused silica. The movement of Stage 2 is associated with the stretching force to elongate the tube. As stage 2 moves to the desired point, the butane torch is removed allowing the tubing to cool down and solidify. The ends of the tubing are released and the final tubing can be picked up on a glass slide or silicon wafer for further use. The two ends still retain their shape since they are fixed on the stage and kept cool. The centre part of tubing, in the heating zone, is deformed, and the inner diameter can be reduced to

submicron dimensions. However, it should be noted that the diameter is not uniform along the capillary (shown in the inset). Importantly, the micro- scale ends can be easily integrated with other components such as reservoirs for feeding in sample solution.

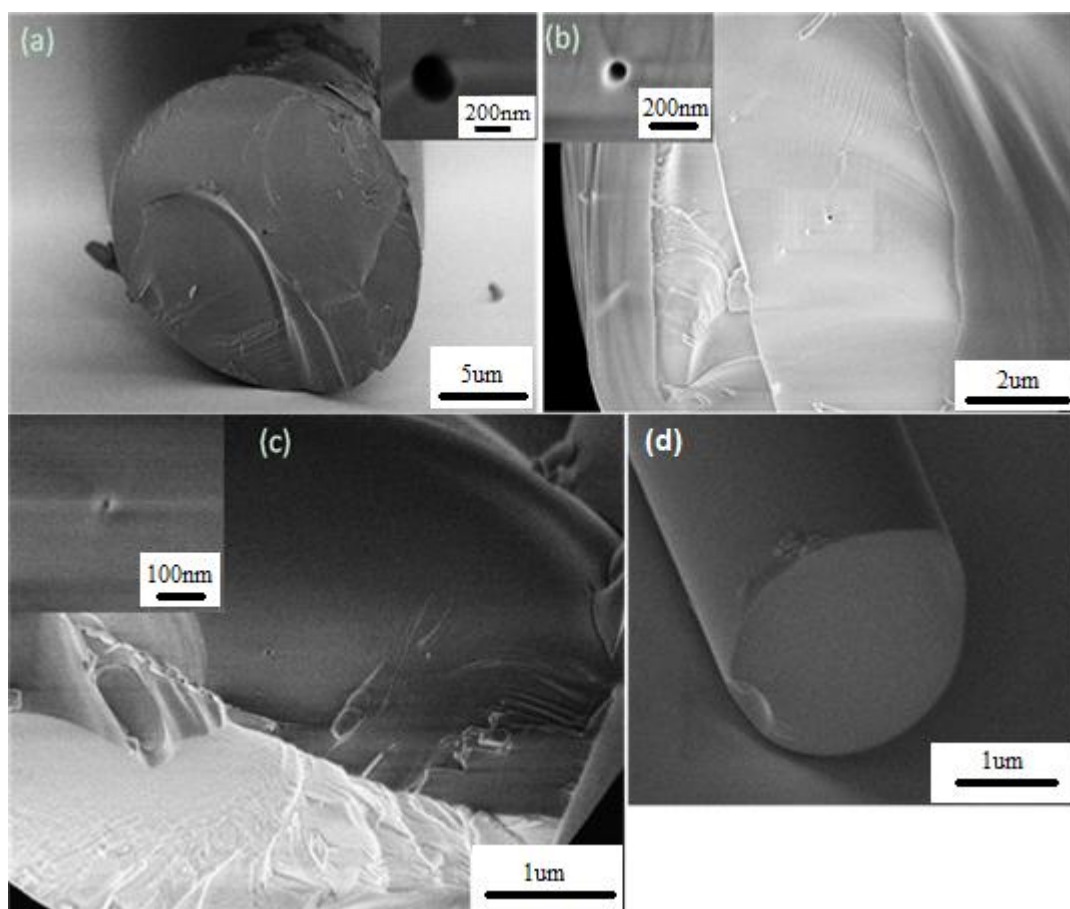


Fig. 12 SEM images of stretched fused silica nanochannels with different shifts of (a) 1 cm (b) 2 cm (c) 3 cm (d) 5 cm.

In following experiments, plastic reservoirs were glued over the channel ends with 5-minute epoxy. To assess their structural integrity, a  $4.9\mu\text{M}$  solution of 5-Iodoacetamidofluorescein (IAF) in a pH=9 EPPS buffer was injected into the reservoir. The solution was infused into the channel by capillary force. The channels were then monitored using fluorescence microscopy. Under normal conditions the sample solution

flows into the channel very quickly. However, the linear velocity decreases dramatically as the solution approaches the centre of the channel where the diameter is the smallest (and sub-micron). The image shown in Fig. 13 illustrates the IAF-filled fused silica nanochannel with a minimum inner diameter of approximately 300nm. This simple visualisation experiment confirms that the heat-induced stretching method can create a continuous nanochannel directly from a microchannel. The advantage of this fabrication method is its simplicity and low cost. Indeed, high throughput fabrication can be achieved if multiple tubes are fixed and stretched together. The primary drawback associated with the technique is related to the fact that the channel dimension is not uniform along the entire length of the conduit. Furthermore, it is difficult to fabricate nanochannels with an internal diameter less than 150 nm.

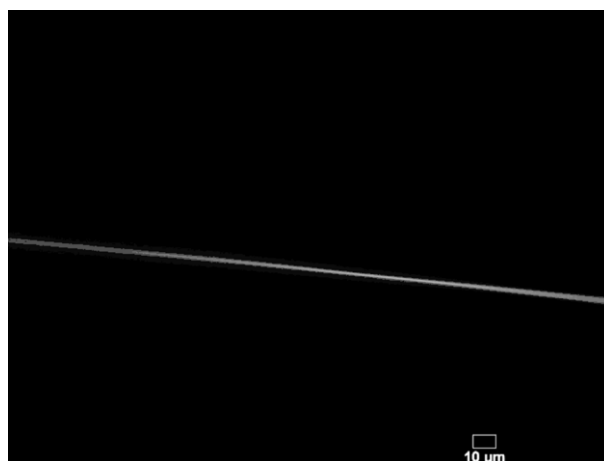


Fig. 13 Fluorescent image of IAF-filled fused silica nanochannel. Fluorescent dyes were drawn into the hollow channel by capillary force. The bright line is the filled channel.

### 3.2 Electrokinetic Analysis of Molecules in Nanochannel

Molecule transport in the photon counting experiments described in section 2.5 relies on capillary force. However, this force is transient and once the channel is filled with solution, molecular transport by capillary forces is replaced by molecular diffusion. To overcome diffusional-induced molecule transport, electrokinetic forces have been employed to transport molecules. On application of an electric potential between the two reservoirs charged ions in the solutions are motivated by the electrophoretic effect, whilst neutral molecules move due to electroosmosis.

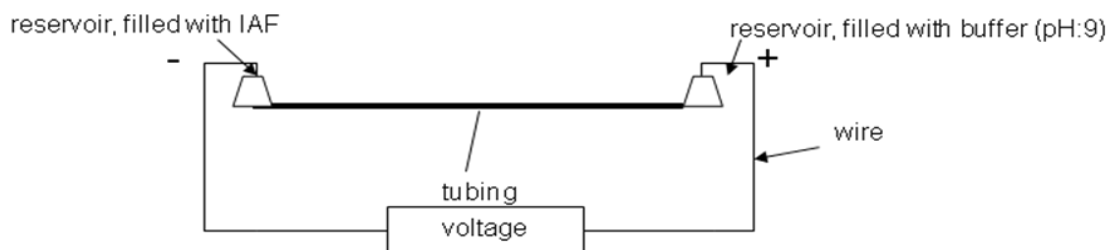


Fig. 14 Schematic diagram of experiment setup for electrokinetic effect in a nanochannel. A hollow nanochannel was deposited on quartz wafer, with two plastic reservoirs attached at two opening ends, respectively. After the channel was fully loaded with sample solution, an external electric field was applied through two electrodes immersed in two reservoirs to initiate the electrokinetic effect. An 800nm-pulsed laser source (two photon excitation) was focused at the center of the channel to excite the fluorophores. Emitted photons were collected by an avalanched diode.

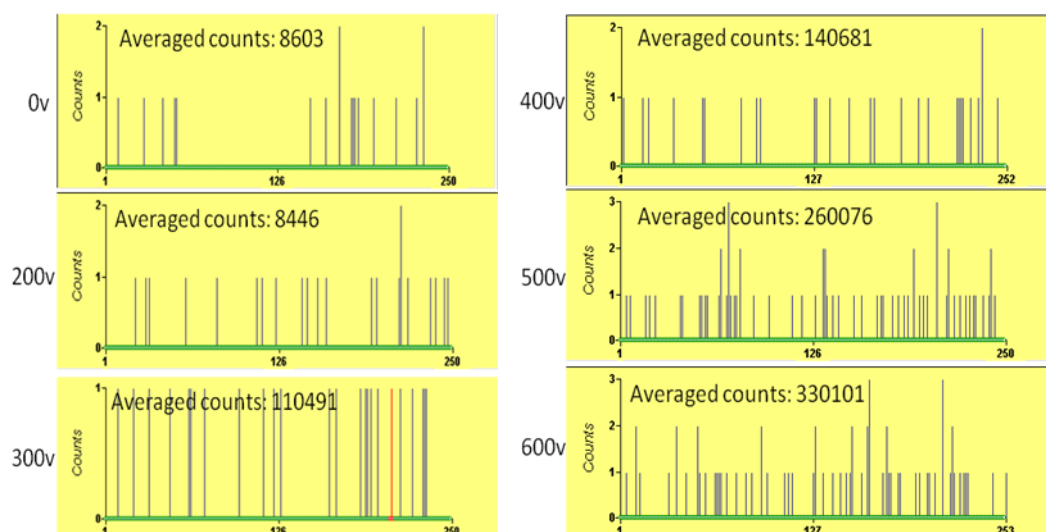


Fig. 15 Photon burst signal monitored over time in a nanochannel under different voltages. Emitted fluorescent photons from IAF were collected by an avalanched diode as the external electric field was changed. The averaged counts are the total photon burst collected in 10 sec. X-axis demonstrates time in a unit of  $\mu\text{s}$ . Y axis shows the number of collected photon counts. From the variance of photon counts under different voltage, the motion of fluorecent molecules in the channel can be analyzed.

The IAF-filled fused-silica nanochannel (200 nm diameter) was used to demonstrate the electrokinetic transport of molecules. A schematic diagram of the set-up is shown in Fig. 14. Two plastic reservoirs were glued at the ends of channel, and a 4.9  $\mu\text{M}$  IAF solution was introduced into the left reservoir for 2 hours until the entire device was filled up with the sample solution. Then EPPS buffer was injected into the right reservoir and an electric field applied across the channel. The excitation laser was focused into the channel, and photon burst counts monitored as a function of applied voltage. Fig. 15 shows the results of this investigation. The averaged counts represent the total photon counts collected over a period of 10 seconds. It can be observed that this number increases dramatically as a function of applied voltage, meaning that more IAF molecules pass through the detection volume within a given period of time. Thus, the transport of molecules in nanochannel can be controlled by an electric field. A plot of

averaged photon counts as a function of applied voltage is shown in Fig. 16. Within the range of 0-200 volts, diffusion dominates molecular transport. As the applied voltage exceeds 200 volts, the electrokinetic force begins to dominate. Indeed, between 200 and 600 volts, the averaged photon counts exhibit a quasi-linear increasing relationship with the applied voltage. Molecular diffusion is still occurring but the electrokinetic force turns is now the main dragging force on target molecules. As the applied potential increases, the relative contribution of the electrokinetic force becomes larger and larger and diffusion effects can be neglected above 500 volts.

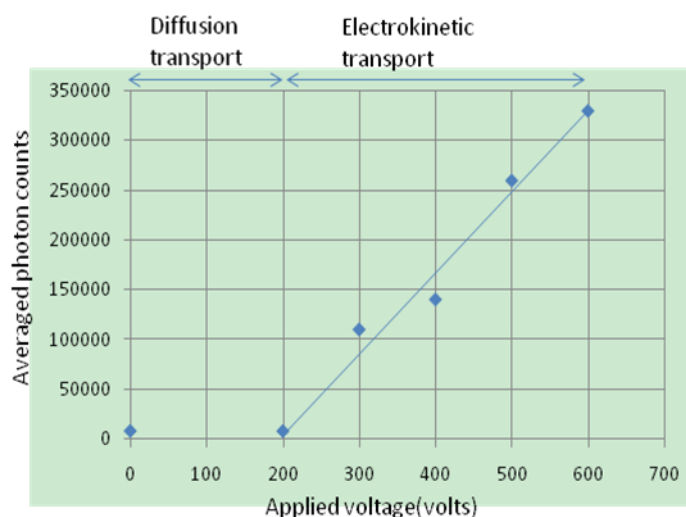


Fig. 16 Averaged photon counts versus applied voltage. The dots in the graph demonstrate averaged counts under different voltage. The diffusion transport range is from 0 volts ~ 200volts, where no much difference was found in the number of averaged photon counts. In the electrokinetic transport range, a straight line is averaged between the lowest voltage (200 volts) and the highest voltage (600 volts). The detected counts at other voltages are evenly distributed along the line.



## 4. NANOCHANNEL DEVICE FOR SURFACE-ENHANCED RAMAN SPECTROSCOPY\*

### 4.1 Introduction of Surface-enhanced Raman Spectroscopy

Raman scattering has been known as the inelastic scattering of incident photons from a molecule since 1920s. It is named the Indian physicist, C. V. Raman. The incident source is a monochromatic light, usually a laser. Considering the light source as a stream of photons, most photons are elastically scattered without change in energy, which is called Rayleigh scattering. A very small fraction of the incident photons, about 1 in  $10^7$ , exchange energy with molecules in the process which is named Raman scattering or Raman effect. The wavelength and frequency of the scattered photons are different from the incident ones. There are two kinds of Raman scattering: Stokes scattering and anti-Stokes scattering. A photon imparts energy to a molecule for Stokes scattering and adsorbs energy from a molecule for anti-Stokes scattering. Both rotational and vibrational Raman spectroscopies are possible, although vibrational Raman spectroscopy is much more widely used. The Raman scattering probes vibrational

---

\* Part of this section is reprinted with permission from “An Optofluidic Device for Surface-enhanced Raman Spectroscopy”, by Miao Wang, Nan Jing, I-Hsien Chou et al. 2007, *Lab on a Chip*, 7, 630-632, Copyright 2007 by The Royal Society of Chemistry. (<http://www.rsc.org/publishing/journals/LC/article.asp?doi=b618105h>)

Part of this section is reprinted with permission from “Nanofluidic Biosensing for  $\beta$ -Amyloid Detection using Surface Enhanced Raman Spectroscopy”, by I-Hsien Chou, Melodie Benford, Hope T. Beier et al. 2008, *Nano Letter*, 8, 1729-1735, Copyright 2008 by American Chemical Society.

Part of this section is reprinted with permission from “Optofluidic Device for Ultra-sensitive Detection of Proteins using Surfaced-enhanced Raman Spectroscopy”, by Miao Wang, Melodie Benford, Nan Jing, et al. 2009, *Microfluidics & Nanofluidics*, 6, 411-417, Copyright 2009 by Springer Science + Business Media.

information of molecules, which are very specific for the chemical bonds in molecules. Therefore, by measuring the intensity of Raman scattering as a function of the frequency of the scattered light, Raman spectroscopy can be established and characteristic information of a molecule can be provided. It is a very useful analytical tool in chemical and biological analysis. However, its application has been greatly limited by its sensitivity. This is due to the relatively low number of Raman scattered photons compared to Rayleigh scattered ones. The Raman scattering cross sections are between  $10^{-31}$ - $10^{-29}$   $\text{cm}^2/\text{molecule}$ .<sup>100</sup> Comparing to the fluorescence process, the cross section of the Raman process is 12-14 orders of magnitude lower.<sup>100</sup> Therefore, in most biological application, broad band fluorescence signals of much higher intensity than Raman signals from molecules creates challenges for obtaining meaningful quantitative Raman signals. Fig. 17 shows the schematic of different processes in a molecular energy level diagram.

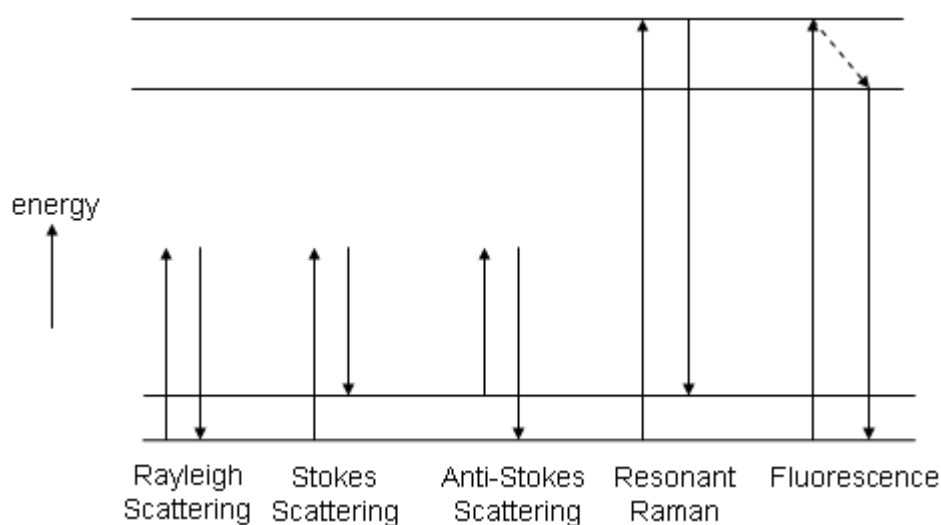


Fig. 17 Schematic diagram of different processes.

In 1974, an unexpected high Raman signals from pyridine on a roughened silver electrode surfaces was reported for the first time.<sup>101-103</sup> This phenomenon was called surface enhanced Raman scattering (SERS) effect and was verified by the detection of many different molecule samples adsorbed on various rough metal surfaces.<sup>104-106</sup> The enhancement in first reports was found to be  $10^3$ - $10^6$ -fold comparing to normal Raman scattering. The enhancement factor in the order of  $10^{10}$ - $10^{11}$  has been reported for dye molecules in surface-enhanced resonance Raman scattering.<sup>107-113</sup> Near-field SERS has demonstrated an enhancement factor of  $10^{13}$ . At certain so-called “hot spots”, the enhancement factor may be possible in the order of  $10^{14}$ - $10^{15}$  in single molecule studies.<sup>114,115</sup>

This enhanced Raman effect attracted extensive attention since the sensitivity of Raman scattering can be greatly improved and possibilities to new potential applications have been opened, such as trace analysis, single-molecule detection, environmental monitoring and diagnostics of certain diseases. There are many excellent articles and reviews about SERS studies.<sup>100,106,116-128</sup> SERS effect has been reported using various so-called “SERS-active” substrates, such as metal-coated nanospheres, silver island films, silver or gold colloids, metal nanoshell, nanorod and nanoparticle array, etc. Some variations of Raman spectroscopy have also been explored, such as Hyper Raman, Resonance Raman, Spontaneous Raman and Optical Tweezer Raman.

## 4.2 Mechanism of SERS

In the first observation of SERS effect on the electrochemically roughened silver electrodes, the roughened silver electrodes play the important role for SERS to occur. Different metals have also been investigated for the SERS activity, including Au, Cu, Pt, Ni, Li, Na, Cd, Al, Zn, Al, Ga, In and alkalis.<sup>129-133</sup> SERS-active substrates can be metal nanostructures, such as nanoshell, nanoparticles, nanorod, or nano protrusions on flat surfaces. Nowadays, silver and gold nanostructures are the most common substrates for their strong enhancement factors and relatively easy preparation. In some biophysical applications, gold is favored for its chemical inactivity.

There are enormous theoretical models and analysis investigated to give a reasonable explanation of the enhancement mechanisms<sup>106,122,123,127,130,134-141</sup>, which, however, have not been well understood yet. From late 1970s, electromagnetic resonances in metal nanostructures, currently named localized surface plasmons (LSPs), were put forward as a major contribution to the enhancement. The electromagnetic theory has been generally accepted as a basic SERS mechanism since it can be a good interpretation for many SERS phenomena including the requirement of nanoscale features of SERS-active substrates, the dependence of enhancement on the size and distribution of SERS-active substrates, the difference of enhancement effect from different metal materials, etc. However, electromagnetic effects do not account for the total enhancement, which has been agreed from the start. Some observations such as the molecular selectivity of enhancement (e.g. No SERS enhancement for methanol<sup>100</sup>) and the dependence of enhancement factor on the electrode potential indicate other

mechanisms. In some cases, for example, the work of Nie et.al<sup>142</sup>, Kneipp et al.<sup>114,115</sup> at single molecule level using SERS, the best estimation of electromagnetic enhancement still leave a gap of two to three orders of magnitude to the observed enhancement. The extra enhancement is possibly due to chemical effects.

In the electromagnetic theory,<sup>137-140</sup> there are two main sources of the enhancement - the enhanced laser electromagnetic field and the amplified molecule radiating Raman field. For the chemical effect, a new Raman process seems to occur for a molecule in contact with a metal nanostructure.<sup>100</sup> This process has a large cross section than the Raman cross section of a free molecule. It was also suggested that the Fermi level of metal lays between the ground state and excited states of the molecule and the transitions among the ground state, excited states and Fermi level are possible.<sup>138</sup> The relative importance of two effects is controversial. But comparing to electromagnetic model, the chemical theory has not been fully developed. And most studies till now show that the value of electromagnetic enhancement is much larger than that of chemical enhancement.

Metal nanostructures have great influence on the enhancement factor of SERS. Metal nanostructures with different sizes and interspacing show optimized enhancement at different frequencies. These effects can be interpreted well by electromagnetic model. For SERS to occur, the metal nanostructures must have a dimension smaller than the wavelength of excitation source to sustain oscillating surface plasmons. Beside the nanoscale roughness for the electromagnetic enhancement, atomic-scale roughness is of importance in the chemical enhancement (first-layer mechanism). The SERS-active

nanostructures usually have a dimension in the range of 5-100nm. And they usually consist of a collection of nanostructures, such as nanoparticle aggregates, rough metal surfaces and island films, etc. Soon after the observation of SERS effect, it was found that the SERS intensity can be greatly increased when two or more nanoparticles are brought close enough. The interaction of particles, or called electromagnetic coupling effect, can bring a giant enhancement which is about six orders higher than that at isolated metal particles. As the spacing between nanoparticles increases, the enhancement falls off rapidly. Detailed explanation of this effect can be found in some articles.<sup>137,140</sup> As more metal nanoparticles are aggregated into large clusters, “hot” sites are created. Particular strong enhancement up to  $10^{12}$  can be found at these hot sites. In practical SERS experiments, the search for hot sites is an important step to obtain large enhancement, and therefore, establish a sensitive detection. However, the hot sites are not distributed uniformly on the SERS-active surfaces. On the entire clusters, the excitation is not uniform and spatially localized at hot sites, which can be as small as a few nanometers. Usually the locations of the hot sites are hard to control and predict with conventional techniques. They depend on the shape and size of the aggregated cluster, the spacing between nanoparticles and the excitation wavelength, and polarization of optical fields. It has limited the reproducibility and applications of SERS. Different techniques have been explored to provide reliable results of SERS. For example, metal nanoparticle-array plates that have periodically aligned nanoparticles on the detection site were investigated as SERS-active substrates.<sup>143-146</sup> A nanoparticle-film with temperature-controllable interparticle spacing was designed as a tunable SERS

substrate to generate the optimal SERS signal intensity.<sup>147</sup> Recently, it was reported that hot nanoparticle pairs can be created by move single silver nanoparticles and form SERS-active silver particle dimmers by using optical tweezers.<sup>148</sup> Different from these techniques, we have designed a novel nanochannel device, which has opened a new method for efficient and reproducible SERS detection. This device consists of a deep-shallow structure and can trap metal nanostructures at a specific predictable location to form hot sites. The device paved a new way for controlled SERS analysis. Details can be found in section 4.4 – 4.6

### 4.3 Overview of SERS-active Substrates

The enhancement factor of SERS is sensitive to the features of SERS-active substrates. Thus one prerequisite of SERS detection is the stability and reproducibility of SERS-active substrates with nanoscale features. How to produce the substrates fast, easily and cost-effectively is of importance. How different substrates affect SERS signals has also attracted enormous interests. Here some typical SERS-active substrates are summarized.

#### 4.3.1 Roughened Metal Electrodes

In the early studies of the SERS effect on silver, gold, copper, platinum electrodes,<sup>101,149-153</sup> an “activation cycle” is necessary for obtaining of strong SERS signals. For the example of silver electrodes:





This cycle is an electrochemical oxidation-reduction cycle to generate surface protrusions with a size from 25nm to 500nm. This kind of substrates can provide an enhancement factor of around  $10^6$ . Its advantage in SERS experiments is that the surface potential can be easily adjusted and the charge transfer processes between the interested molecules and metal electrodes can be investigated.

#### 4.3.2 Metal Island Films

Metal island film<sup>154-159</sup> is a very thin metal layer, usually less than 10 nm on a solid base substrate. It can be produced by thermal/e-beam evaporation or sputtering deposition. Slow rate of the deposition can generate island films instead of continuous films. Gold and silver vacuum-deposited island films have been characterized by studying deposition variables such as film thickness, evaporation rate, and substrate temperature. These parameters were correlated with SERS effects.

In the comparison of silver, gold and copper for the enhancement in SERS experiments, silver shows the best performance, followed by gold and copper. But gold has the advantage of chemical inactivity and the enhancement of gold is comparable to that from silver when near-infrared excitation is used.

#### 4.3.3 Metal Colloids

Silver and gold colloids are widely used in these years for their relatively easy preparation and good performance in enhancement. They are usually in a manner of



aggregated clusters of colloidal silver or gold particles with a dimension in a range of 10 to 100 nm. The effect of aggregation on the SERS activity of metal colloids was originally demonstrated by Creighton et al.<sup>160</sup> These colloids can be used in solution or dried on a surface. In the detection of aqueous samples, an active agent, such as sodium chloride, is often used to initiate the aggregation of the colloids in order to shift the extinction band. These colloids are made by different chemical reduction processes. Silver colloids are generally produced by reduction of silver nitrate with sodium citrate (Lee-Miesel method<sup>161</sup>), or by reduction of silver nitrate with sodium borohydride. Recently, a new method was claimed as reduction of silver nitrate with hydroxylamine hydrochloride at alkaline pH at room temperature.<sup>162</sup> The advantage of this method is the fast preparation and immediate applicability for SERS. The size and dispersion of the produced colloids can be controlled by changing the mixing order and rate of the involved solutions.

In conventional SERS experiment, the interested molecules are mixed with silver or gold colloids with active agent to generate closely spaced aggregates. The molecules are adsorbed on the surface of colloids. The sample can be in solution or dried on a surface. At certain hot sites, strong SERS signal can be collected.

Efforts have been made to produce more uniform and controllable SERS substrates rather than colloidal suspensions. Metal nanoparticle arrays are investigated for the interacting effect between particles for the optimized enhancement.

#### 4.3.4 Metal Nanoparticle Array

Regular metal nanoparticle arrays have been fabricated by e-beam lithography with control over particle size, shape and distribution.<sup>143,144,163-165</sup> It was reported that the surface plasmon resonances of these nanoparticles can be located at any desired wavelength from visible to near-infrared region through the control of the geometrical features of nanoparticles.<sup>163,165</sup> According to the electromagnetic theory, surface plasmon resonances are dependent on the size, shape, distribution of nanoparticles and the substrate and medium dielectric function. Optimized SERS signal can be obtained when the wavelength of surface plasmon resonance approaches the wavelength of excitation as well as that of Raman lines.<sup>163, 165-167</sup> The flexible control of particles geometry through fabrication process has enabled the tuning of surface plasmon resonances to maximize the SERS signal. The experiment results on gold nanoparticle arrays on indium tin oxide (ITO) coated glass with an enhancement factor of  $\sim 10^5$  have been reported with good consistence with this theory.<sup>163,165</sup> The extinction spectrum of the array is sharp in this study. An interesting feature is that the Raman gain does not depend on the extinction coefficient of the array.<sup>163</sup> The phenomenological relation given by Weitz and co-workers<sup>168</sup> was used to explain this result.

The base substrate for nanoparticle array also affects the SERS signal. ITO-doped glass substrate and smooth gold film with tens of nanometer thickness were compared.<sup>164</sup> The gold nanoparticle arrays deposited on gold film display two plasmon bands instead of single one observed on ITO-glass. By changing the film thickness and the interparticle spacing, two bands overlap with each other and generate a broad

plasmon band. With gold film as substrate, the enhancement factor of gold nanoparticle arrays rises up to  $10^8$ . The intriguing results have initiated the fabrication of “sandwich films” which have a dielectric layer between the particles and gold film.

Nanoparticle arrays with extremely small interparticle spacing (smaller than 10 nm) have also been proposed.<sup>143</sup> Cetyltrimethylammonium bromide (CTAB)-capped gold colloids with a diameter of 50nm in solution was dried on ITO-glass and produced hexagonally monolayer gold nanoparticle arrays with an interparticle spacing of ~8nm. A broad plasmon band in the near infrared region was found and attributed to the dimer plasmon resonances. The advantage of this array is the uniform densities of hot sites because large SERS enhancement can be achieved between neighboring nanoparticles when the excitation wavelength approaches the maximum of the broad plasmon feature. An enhancement factor above  $10^8$  was claimed with an excitation at 785nm.

#### 4.3.5 Metal Nanorod/Nanowire Array

Substrates consisting of silver or gold nanorod arrays have been reported as SERS-active substrates in recent years. These nanorods can be mounted on various substrate, such as silica,<sup>169</sup> optical fibers<sup>170</sup> and linear-polyethylenimine-modified tin oxide substrate.<sup>171</sup> A preliminary paper about using nanorods as SERS-active substrate was reported in 1995.<sup>172</sup> Silver nanowires were produced by silver deposition in anodic aluminum oxide (AAO) nanotemplates and subsequent partial removal of the oxide layers. The wires can be fabricated with lengths in excess of 2  $\mu\text{m}$  and with diameters between 10 to 200 nm. But the SERS signals from these nanorods were not as good as

that from normally prepared silver colloids and did not attract much attention. Later on, nanorods of different metals fabricated using similar procedure have been tried as SERS-active substrate including Cu, Ag, Au, Ni and Co.<sup>173</sup> The resultant nanorods arrays were investigated using atomic force microscope (AFM) and transmission electron microscope (TEM). The diameters ranged from 15 to 70nm. The intriguing result is that besides the noble metals - Cu, Ag and Au, transition metals – Ni and Co - also show an enhancement factor of around  $10^3$ .

Detailed SERS studies on silver and gold nanorods were reported a few years ago.<sup>169,174</sup> Theoretical analysis and experiment results both indicate that an optimal enhancement depends on the nanorods aspect ratio,<sup>175</sup> the density and spacing. Monodispersed gold nanorods and aggregated gold nanospheres on silica surface were compared as SERS-active substrates using 2-aminothiophenol (2-ATP) as targeted molecules.<sup>169</sup> Gold nanorods demonstrated a comparable or even better performance over Gold nanospheres under similar experimental conditions. By an oblique angle deposition, silver nanorods with different length ranging can be fabricated on glass substrate.<sup>174</sup> The silver nanorods achieved the optimal enhancement factor of  $10^8$ , which is a rival for conventional colloidal particles.

Silver nanorods arrays have been explored for the rapid and sensitive detection of respiratory virus molecular signatures, which was reported in 2006.<sup>176</sup> With the larger enhancement factor, the rapid determination of Raman spectra of small amount and low concentration of viruses is possible. Since the information provided by Raman spectra is

specific for each virus, this technique is not only a diagnostic tool, but also can be used as a means to track the origin and variation of viruses.

#### 4.3.6 Metal-Coated Nanoparticles and Metal-Film-Over-Nanospheres (MFON)

Metal-coated nanoparticles and Metal-film-over-nanosphere (MFON) are also SERS-active substrates.<sup>177-186</sup> It consists of a base support, a layer of nanoparticles/nanospheres on the base, and a metal film - usually silver or gold - coated over the nanoparticles/nanospheres layer. The nanoparticles can be made of different materials, such as silica,<sup>182</sup> titanium dioxide,<sup>183</sup> alumina,<sup>184</sup> polystyrene latex,<sup>185</sup> etc.

The basic fabrication procedure includes the coating of nanoparticles/nanospheres on the base support, followed by a deposition of a thin metal film less than 100nm. It was also reported that metal nanoparticles can be immobilized onto the first nanoparticle layers on the base.<sup>182</sup> Similar to metal nanoparticle arrays, the size and interspacing of the nanospheres can be adjusted for maximized enhancement. The thickness of the top metal layer also has an influence on the enhancement factor.

In the comparison with flat metal film and roughened metal film, metal-coated nanoparticles and MFON provided the strongest Raman enhancement and lowest background noise. More importantly, the enhancement show less dependence on the position of detection, which means a relatively uniform hot site distribution.<sup>182</sup> This kind of substrate has also been coupled with electrodes (e.g. MFON electrodes) and compared with conventional electrochemically roughened electrodes.<sup>185</sup> The advantage of MFON

electrodes over conventional ones presents as a lossless enhancement upon excursion to extremely negative potentials

#### 4.3.7 Metal Nanoshells

Typically, metal nanoshells consist of a dielectric core and a thin silver/gold coating.<sup>186-192</sup> Metal cores have also been investigated.<sup>190</sup> Different from metal colloids, metal nanoshells present a more “individual” contribution to the SERS enhancement. The plasmon resonances of the nanoshells can be altered in a wide range from visible to near-infrared wavelength by appropriate selection of inner core size and outer shell thickness.<sup>186-189</sup> The electromagnetic responses from the nanoshells can be calculated by various methods such as the classical Mie scattering theory<sup>193</sup> and finite difference time domain methods<sup>194</sup>. Beside the core-shell structure, it was suggested that the density of the metal network also gives additional contribution to the enhancement.<sup>186</sup> The maximum enhancement was observed from the nanoshells with a dense but incomplete metal coating rather than completely sealed nanoshells. To investigate individual contribution from nanoshells to the enhancement, the SERS intensity was measured as a function of nanoshells density on a base substrate. The linear increase of the intensity with nanoshell density indicates that the SERS response is from single nanoshell resonance and no extra enhancement is related to dimmer plasmon resonance. Gold nanospheres, nanoshells, nanospheres and nanoshells dimmers were compared.<sup>189</sup> The enhancement from nanoshells can be comparable to that from nanosphere dimmers.

#### 4.3.8 Other Nanostructured SERS-active Substrates

SERS activity has also been observed on other non-conventional substrates. Some new substrates have also indicated new applications of SERS. For example, with an optical fiber coated with SERS-active substrates, SERS signals can be collected through the fibers for probing.<sup>195</sup> With their fine structure, AFM and STM tips have also been used as SERS-active substrates.<sup>196-202</sup> SERS signal can be measured when the tip approaches a layer of target molecules within a few nanometers. The intriguing part of the tip is that a single hot site can be provided at the tip end. But the excitation wavelength should be chosen wisely for a given tip geometry to optimize the enhancement.

Other than metal nanorod/nanowire array, metal nanorod/nanowire layer-by-layer films also show satisfying enhancement of SERS.<sup>171,203</sup> A sandwich structure of metal-targeted molecules-metal has been investigated.<sup>204,205</sup> The enhancement is affected by the interlayer distances, dimension and material of top and bottom metal layer.

Sputtered silver oxide layers also presents SERS effect after photoactivation.<sup>206</sup> Micro/nanochannel devices have recently been investigated to study and improve SERS effect. Nanowell surfaces in microchannel biochips<sup>207</sup> and alligator teeth-shaped PDMS microchannel<sup>208</sup> have been reported. In the following sections, an innovative nanochannel trapping device is discussed, including its design, fabrication and applications. This nanochannel can provide highly improved detection sensitivity and reproducibility of SERS and has been used as a powerful platform in biomedical applications, such as biomarkers identification for disease diagnosis.

#### 4.4 Design and Fabrication of Nanochannel Trapping Devices

In the detection of SERS signal, target molecules are adsorbed onto SERS-active nanostructures. However, because of the non-uniform distribution of hot spots, it is especially challenging to get controllable and consistent enhancement. This inconsistent enhancement is one of the reasons that SERS could not provide reliable and reproducible results in the past. In addition, target molecules are randomly adsorbed on the nanoparticle clusters. This means that the probability that target molecules are confined in a hot spot is low. These problems have limited the expansion of SERS applications. To improve the SERS technique, there are some new investigations underway. For instance, as discussed in section 4.3, metal nanoparticle-array plates that have periodically aligned nanoparticles on the detection site were investigated as SERS-active substrates in an effort to provide reliable results. However, these approaches take long time for molecules adsorb on the SERS active site and the molecular distribution on the SERS active site at low sample concentration is still not uniform, which limits SERS detection sensitivity.

To overcome these problems, a novel nanochannel device is developed to improve the sensitivity of SERS detection. This device has a pinched micro-nanochannel step structure where metallic nanoparticles and target molecules in aqueous solution can be consistently trapped to form nanoparticle-molecule SERS clusters using the capillary force in the channel.

The nanochannel device can be fabricated on a 500  $\mu\text{m}$ -thick double-side-polished borosilicate wafer or fused silica wafer using photolithographic and etching



processes. The device has a step structure consisting of a deep microchannel and a shallow nanochannel. The deep microchannel has a 20 $\mu\text{m}$  width and 3 $\mu\text{m}$  depth. The shallow channel has a 40 nm depth, 2 $\mu\text{m}$  width, and 40  $\mu\text{m}$  length, which is used for trapping metallic nanoparticles with a size larger than 40nm at the microchannel–nanochannel junction. The width and depth of microchannel as well as the width of nanochannel can be controlled by changing the design on the mask and the etching step accordingly in the fabrication process. With a device fabricated on fused silica wafer as an example, the fabrication process flow chart is shown in Fig. 18. Initially, the first layer of photoresist was spin-coated on the substrate and a 2  $\mu\text{m}$ -width trench was patterned. It was then etched down to 40 nm-depth with dry etching. Then the photoresist was stripped off and a layer of amorphous silicon (A-Si) was deposited onto the wafer using plasma-enhanced chemical vapor deposition (PECVD) to serve as a hard mask. A second layer of photoresist was spin-coated on the top of A-Si layer. The microchannel mask was then aligned with the nanochannel, patterned and developed. A-Si layer was removed by selectively removed by carbon tetrafluoride ( $\text{CF}_4$ ) reactive ion etching and concentrated hydrofluoric (HF) acid (49%) was used to create a 3  $\mu\text{m}$ -depth microtrench. After removing the remaining A-Si layer and photoresist, the inlet and outlet holes were sand-blasted through with fine alumina powders. Finally, the wafer was thoroughly cleaned and clung with an intact fused silica wafer using de-ionized water and annealed at 1050  $^\circ\text{C}$  for 6 hours for permanent bonding. Plastic reservoirs were then attached around the inlet and outlet respectively using 5-minute epoxy. A detailed process flow can be found in Appendix B.

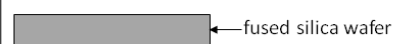
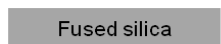
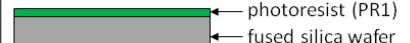





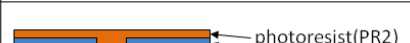







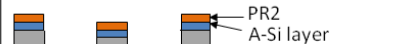





Side View	Top View	Fabrication Flow
 ← fused silica wafer	 Fused silica	4" fused silica wafer
 ← photoresist (PR1) ← fused silica wafer	 PR1	Spin coat photoresist (PR1)
 ← PR1 ← fused silica wafer		UV exposure and develop
 ← PR1 ← fused silica wafer		Dry etch to 40nm
 ← photoresist(PR2) ← A-Si layer ← fused silica wafer	 PR2	Strip of PR1, PECVD deposited A-Si layer and spin coat a 2 <sup>nd</sup> layer PR2
 ← PR2 ← A-Si layer ← fused silica wafer		Align, pattern and develop
 ← PR2 ← A-Si layer ← fused silica wafer		Remove A-Si layer by CF <sub>4</sub> reactive ion etching
 ← PR2 ← A-Si layer ← fused silica wafer		Wet etch to 3μm
 ← fused silica wafer		Remove PR & A-Si layer
 ← fused silica wafer		Sand blasting inlet and outlet holes
 ← fused silica wafer		Bond with another wafer

Fig. 18 Process flow chart of the fabrication process of nanochannel device.

The schematic diagram of the nanochannel device is shown in Fig. 19 (a) and (b). The cross section of nanochannel (after the process wafer bonded with an intact one) is shown in Fig. 19 (c). The nanochannel has a depth of 40nm. The microchannel has a depth of 3 μm and a width of 50 μm. However, because of the isotropic HF wet etching, the sidewall of microchannel is not straight. The width of microchannel decreases as the depth goes deeper. The smallest width is realized at the microchannel bottom, which is about 50 μm, as shown in Fig. 19 (d).

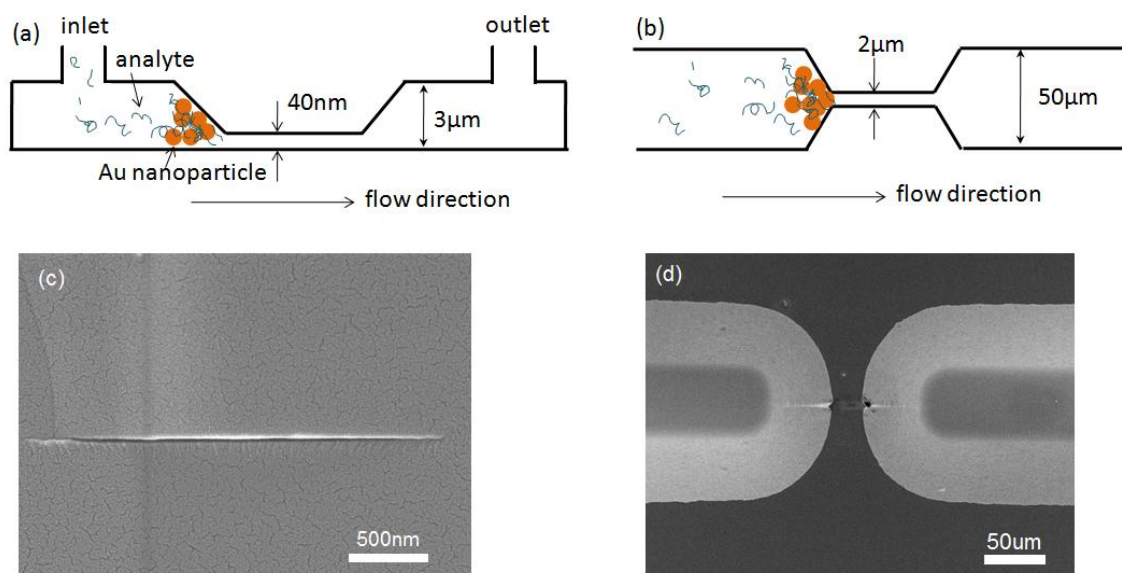


Fig. 19 (a) Schematic diagram of a nanochannel device (side view) (b) Schematic diagram of a nanochannel device (top view) (c) SEM image of nanochannel cross section (d) SEM image of a nanochannel device (top view).

In our experiment, gold nanoparticles with a diameter of 60 nm suspended in water were used as the SERS-active metal nanostructures. The gold nanoparticles were mixed with analyte solution and then dispensed into the inlet reservoir. The sample solution was drawn into the nanochannel device by capillary force. Since the size of gold nanoparticles is larger than the depth of nanochannel, gold nanoparticles were trapped and formed into clusters at the entrance to the nanochannel. Furthermore, capillary force continued to bring analytes through the interstices of the gold clusters and created an area with locally high concentration of analytes around the gold clusters. The highly condensed gold clusters and high concentration of analytes contributed to especially high detection sensitivity.

While the depth of the nanochannel assures the reliable trapping of nanoparticles, the width of the nanochannel was designed to be 3  $\mu\text{m}$  to guarantee fast transportation of aqueous solution. The trapping process occurred within minutes after the sample solution was put into the inlet reservoir. Fig. 20(a) and (b) shows the optical images of aggregation of gold nanoparticles over time. As the nanoparticles were trapped at the junction of microchannel and nanochannel, they formed into clusters as depicted by the black spot shown in the figure. A scanning electron micrograph (SEM) image around the nanochannel entrance is shown in Fig. 20(c). It is obvious that the majority of the gold nanoparticles are aggregated and located at the entrance to nanochannel.

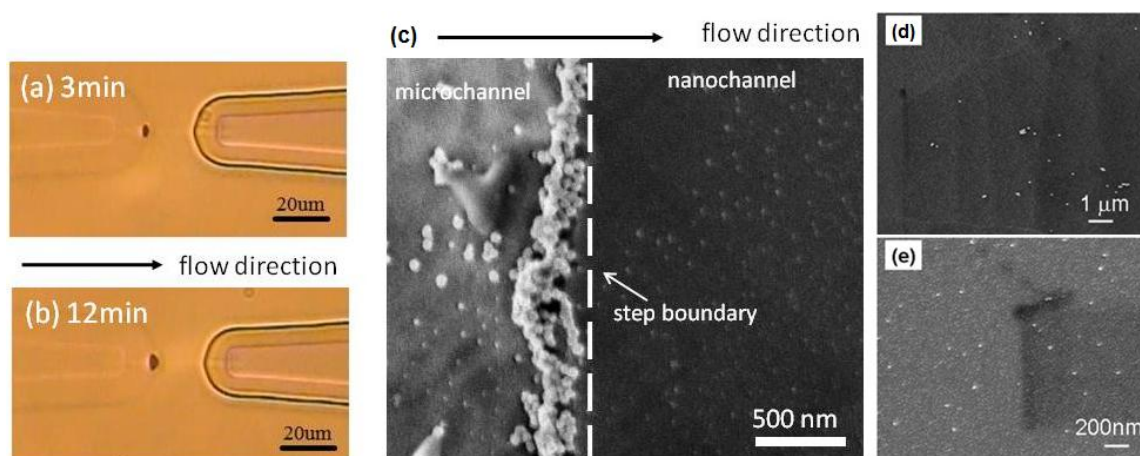


Fig. 20 (a)(b) Optical microscopic images: aggregation of Au nanoparticles monitored over time (c) SEM image of gold nanoparticles aggregation at the boundary of microchannel and nanochannel (top view) (d) SEM image of gold nanoparticles in microchannel (top view) (e) SEM image of nanochannel area (top view).

A few isolated gold nanoparticles were found in the deep channel, however, these nanoparticles were highly scattered, as shown in Fig. 20 (d). These clusters are also out of the detection area for the Raman microscope system and thus they do not

contribute to SERS signal. Some nanoparticles/debris with a diameter smaller than the depth of nanochannel passed through the step and entered the nanochannel, which are shown in Fig. 20 (e).

Fluorescent testing was also performed to confirm the nanochannel trapping performance. Fluorescent polystyrene (PS) nanoparticles in aqueous solution (Spherotech Inc., IL) with a size ranging from 40 nm~90 nm were introduced into the nanochannel device. Since the diameter of the fluorescent nanoparticles is larger than the depth of shallow nanochannel, they were trapped at the nanochannel entrance. The solution of PS beads was diluted to 5mg/l using deionized (DI) water and then introduced into the nanochannel from a reservoir. Due to capillary force, the solution was transported into the device within a few seconds. The fluorescent image of PS particles trapped at the entrance of the nanochannel is shown in Fig. 21 immediately after the solution's dispersion. The PS particles emitted extremely high fluorescent signals around the entrance compared to other locations in the microchannel region.

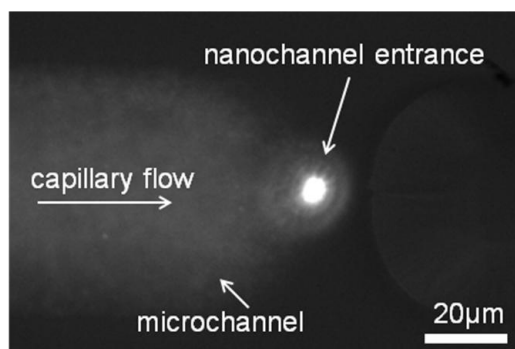


Fig. 21 Fluorescent image of polystyrene nanoparticles trapped at the step boundary of the nanochannel device.

## 4.5 Experiment Results

### 4.5.1 Enhancement Factor and High Sensitivity

To assess this device, the enhancement factor of these nanoparticle clusters were estimated and compared to other SERS techniques using adenine as an analyte. The excitation laser was focused at the nanochannel entrance to obtain the surface enhanced Raman spectra of adenine molecules. SERS detection was accomplished using a Renishaw System 1000 Raman Spectrometer coupled to a Leica DMLM microscope (Schaunberg, IL). The excitation laser source had a wavelength at 785 nm and a power of 8mW at the sample. 50x objective lens was used with a spot size of 2.2  $\mu\text{m}$ . The integration time was set to be 2 minutes and the wave-number range was from 504  $\text{cm}^{-1}$  to 1076  $\text{cm}^{-1}$ .

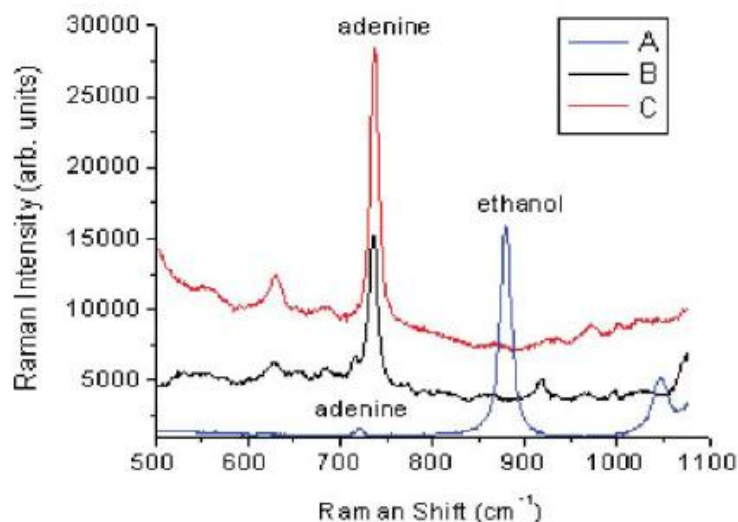


Fig. 22 SERS signals of adenine molecule obtained by different techniques (A) Raman signal without SERS active clusters, (B) SERS active clusters made by the conventional chemical method, (C) SERS active clusters created in a nanochannel device.

There are three signals of adenine molecules shown in Fig. 22. For reference, graph A shows the Raman signal from a solution of 22mM adenine on a glass surface without any nanoparticles. It is diluted in a mixture of ethanol and DI water. The concentration of ethanol is 10.4M. Both adenine and ethanol's peak are demonstrated in the spectrum. The intensity of the signal with arbitrary units shows the fingerprint peak at  $735\text{ cm}^{-1}$  for adenine. Graph B shows the signal from a solution of  $20\text{ }\mu\text{M}$  adenine using a conventional colloidal gold SERS technique. The sample was prepared by mixing 0.5 M sodium chloride, which is an activation agent to make the gold nanoparticles aggregate.<sup>102,114,164,209,210</sup> After the mixing process, the sample sat for 15 minutes to allow for the gold nanoparticles to aggregate forming clusters. Graph C shows the Raman signal from  $20\mu\text{M}$  adenine with the use of a nanochannel trapping device. The sample was a mixture of  $20\text{ }\mu\text{M}$  adenine and gold nanoparticles with a volume ratio of 1:5. The final concentration of adenine in the sample was  $3.33\text{ }\mu\text{M}$ . Immediately after the sample was drawn into the channel via capillary force after the mixing process, the SERS signal was detected. As depicted, the SERS signal from the nanochannel trapping device is the highest of the three SERS approaches. With graph A as a reference, the enhancement factor of the nanochannel trapping device was calculated to be  $10^8$ . The device used for this experiment had a nanochannel with  $25\text{ }\mu\text{m}$  width and  $40\text{ nm}$  depth and a microchannel with  $150\text{ }\mu\text{m}$  width and  $6\text{ }\mu\text{m}$  depth.

#### 4.5.2 The Effect of Molecule Enrichment

The SERS signal as the function of time has been investigated to calculate the molecule enrichment effect at the nanochannel entrance. Due to the continuous capillary flow, the concentration of nanoparticles as well as analytes are increased over time. The concept is that, after the nanoparticle-molecule SERS clusters are formed at the entrance of nanochannel, nanoparticles and molecules continue to flow into the nanochannel entrance due to continued capillary force. Thus, the density of nanoparticles increases. In addition, because of high surface to volume ratio of the SERS active clusters, more molecules tend to adsorb onto the surface of clusters. These effects raise the SERS signal intensity.

To demonstrate this molecular and nanoparticle enrichment effect, we monitored the SERS signal of adenine over time. The trapping effect of gold colloids and molecules can be stably maintained and increase within 30 minutes after loading the sample solution into the reservoir. SERS signals of adenine molecules was measurable with a high signal to noise ratio to a concentration as low as 10 pM. The integration time of the Raman system was set to 1 minute throughout these experiments. The formation of gold clusters with dimension more than 10  $\mu\text{m}$  was observed after the sample solution dispersion. Fig. 23(a) shows the enhanced Raman signal from a 10 pM adenine solution monitored over 30 minutes after loading the sample solution into the reservoir. Capillary force transported gold nanoparticles and adenine molecules into the nanochannel entrance. Fig. 23(b) shows how the SERS signal intensity of adenine changes over time. Two adenine samples at different



concentrations, 50 nM and 10 pM, were investigated. The signal from the 50 nM adenine sample increased and was saturated after 15 minutes. The SERS signal intensity of a 3.3  $\mu\text{M}$  adenine concentration, immediately after loading the adenine solution into the device, is shown as the solid curve in the graph. As depicted, the signal from 10 pM adenine surpassed that of 3.3  $\mu\text{M}$  adenine after 15 minutes. From this, we can reasonably conclude that the enrichment of gold nanoparticles and adenine near the entrance of the nanochannel is increased over time.

After 25 minutes, there is no obvious increase in the concentration because the arriving of molecules and diffusion of molecules has reached an equilibrium state. By comparing the final SERS signal intensity of 10 pM adenine to the reference line of 3.3 mM adenine, we can conclude that a more than  $10^5$  fold increase due to enriched nanoparticle–molecule concentration can be accomplished by this nanochannel.

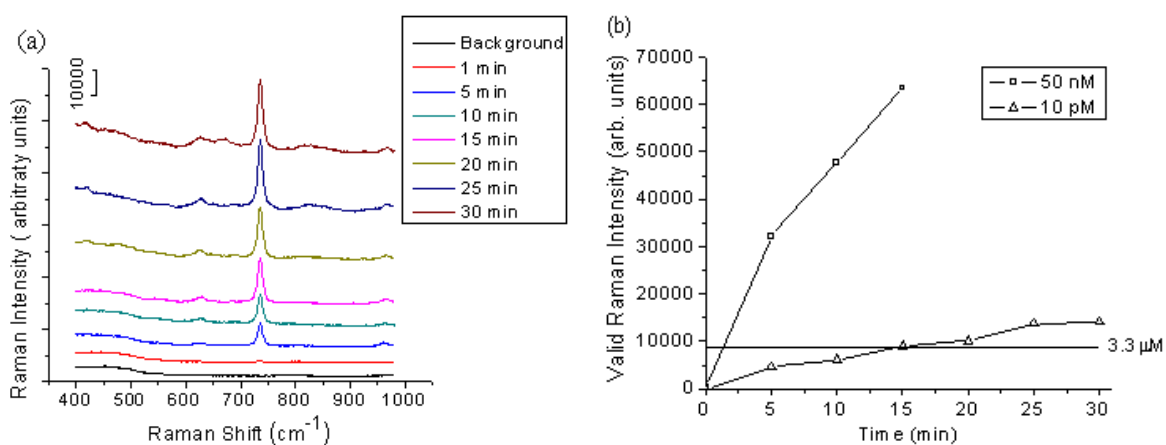


Fig. 23(a) SERS signal from 10 pM adenine collected at different time after the loading of the sample. (b) SERS signal from 10 pM adenine and 50 nM adenine monitored as a function of time.

#### 4.5.3 The detection of multiple analytes

In many applications, the sample of interest has a complex environment containing enormous analytes. It would be very useful if the fingerprint information can be obtained and identified from every analytes. As a preliminary test of the capability to detect multiple analytes using this nanochannel device, a mixture of 1 $\mu$ M adenine, 1mM congo red and Au nanoparticles in DI water (Polysciences Inc., PA) at a volume ratio of 1:1:10 was used as a detection sample. The final concentration of adenine and congo red in the sample is 83nM and 83 $\mu$ M, respectively. The solution was dispensed into the nanochannel device (fabricated on fused silica wafer) immediately after prepared. It was drawn into the channel via capillary force within minutes. Fig. 24(a) shows the compound SERS spectra of adenine and congo red in the nanochannel device monitored over time. The detection spot was focused at the entrance to the nanochannel with a 50x objective lens. The excitation wavelength is at 785nm. The collection time is 30 sec. Adenine shows a characteristic peak at 735 $\text{cm}^{-1}$  while congo red has peaks at 1155 $\text{cm}^{-1}$ , 1286 $\text{cm}^{-1}$ , 1455 $\text{cm}^{-1}$  and 1593 $\text{cm}^{-1}$ . For comparison, the spectrum detected using conventional SERS technique is also shown in the Fig. 24(a) and magnified in Fig. 24(b). The conventional detection used NaCl as an agent to initiate the aggregation of Au colloids, with adenine and congo red at the same concentration. The solution sat for ~15 min to form the aggregated cluster and the spectrum was obtained using a water immersion lens. The characteristic peaks from both molecules, adenine (735  $\text{cm}^{-1}$ ) and congo red (1155  $\text{cm}^{-1}$ , 1284  $\text{cm}^{-1}$ , 1455  $\text{cm}^{-1}$ , 1593  $\text{cm}^{-1}$ ), are identified and enhanced comparing to the SERS signal obtained by the conventional technique.

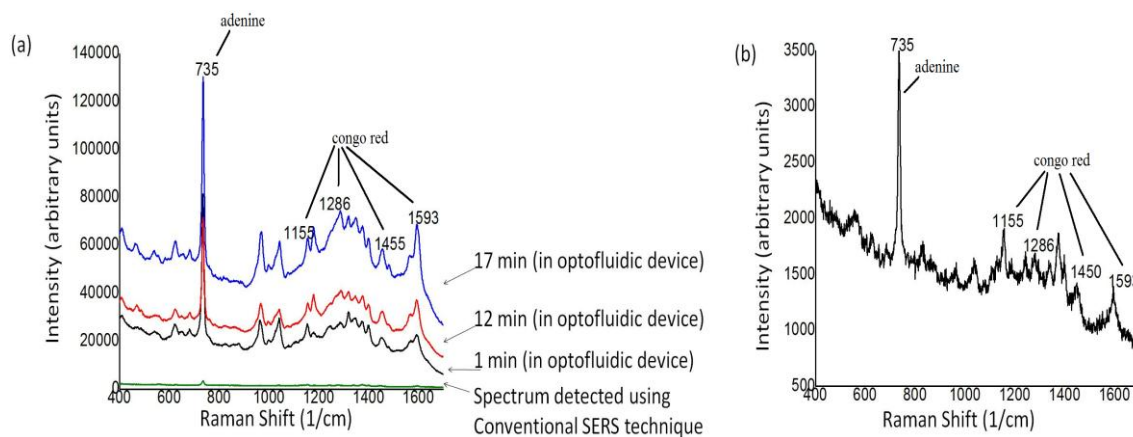


Fig. 24 (a) SERS spectra of 83nM adenine and 83 $\mu$ M congo red monitored in a nanochannel device over time (b) Magnified SERS spectrum detected using conventional SERS technique.

The spectra detected at 1 minute, 12 minutes and 17 minutes after adding sample were shown in Fig. 24(a). This means that the local concentration of both molecules is increased due to continuous capillary force. This result confirmed the potential of nanochannel device to be used in a complex sample detection.

#### 4.6 Application Examples

Since this nanochannel device is powerful in providing structural information of analytes, it has wide application in bio/chemical analysis, such as disease diagnosis and water pollutant detection. Here are some examples of the applications.

##### 4.6.1 Detection of Biomarker of Alzheimer's Disease

Alzheimer's disease (AD) is a progressive neurodegenerative disease and the most common form of dementia.<sup>211</sup> In worldwide, about 26 million people are suffering

from AD. Alzheimer's disease is characterized by loss of neurons and synapses in the cerebral cortex and certain subcortical regions. Although its cause is not fully understood yet, the "amyloid cascade hypothesis" is the most widely discussed and researched hypothesis. The accumulation of abnormally folded beta amyloid ( $A\beta$ ) in the brain are believed to be associated with neurodegenerative changes.<sup>212</sup> Currently, there is no single test that accurately diagnoses AD. It can only be diagnosed definitively by identification of neuritic plaques and neurofibrillary tangles in brain tissue under a microscope, a procedure conducted almost exclusively autopsy. A non-invasive pre-mortem technique for diagnosing AD is in great need for its treatment and prevention.  $A\beta$  from cerebrospinal fluid (CSF) may be good biological biomarkers in the early diagnosis of AD. However, there is no reported fingerprint information of  $A\beta$ . One reason may be the lack of detection techniques. The concentration of  $A\beta$  in CSF is in nano-molar range. It is hard to identify  $A\beta$  at such a low concentration in a complex environment. Moreover, the most prevalent species of  $A\beta$  present in people with AD, which are  $A\beta$  (1-40) and  $A\beta$  (1-42), are found in cerebrospinal fluid (CSF) and blood plasma of all people, regardless of health.<sup>213</sup>

There are many investigations suggesting that the neurotoxicity of  $A\beta$  is associated with its aggregation and change in secondary structures.  $A\beta$  monomer, which is nontoxic and soluble with  $\alpha$ -helical and random coil structure, can misfolded and aggregated into cytotoxic  $A\beta$  with abundant  $\beta$ -pleated sheets (i.e.,  $A\beta$  fibrils and protofibrils).<sup>214-216</sup>

SERS is a possible technique for detecting the conformational change of protein. However, the application of SERS in the diagnosis of AD was limited because of the inconsistency and relatively low enhancement of conventional SERS detection technique. In the previous section, the nanochannel device was demonstrated and proved its capability to significantly improve the reproducibility and sensitivity of SERS by exclusively localizing nanoparticles and increasing the concentration of target molecules at the entrance to the nanochannel. With these advantageous traits, it was used as a SERS platform for the ultimate goal of facilitating diagnosis and understanding of Alzheimer's disease through the detection of Raman spectra that are conformation dependent and unique to A $\beta$  refolding from  $\alpha$ -helical to  $\beta$ -sheet structure. We successfully observed A $\beta$  in different conformational states during the A $\beta$  self-assembly process as well as to distinguish A $\beta$  from confounder proteins commonly found in cerebral spinal fluid. The SERS spectra of A $\beta$  at ultra-low concentrations are shown in Fig. 25 and Fig. 26. Details of the illustration can be found in reference 213.

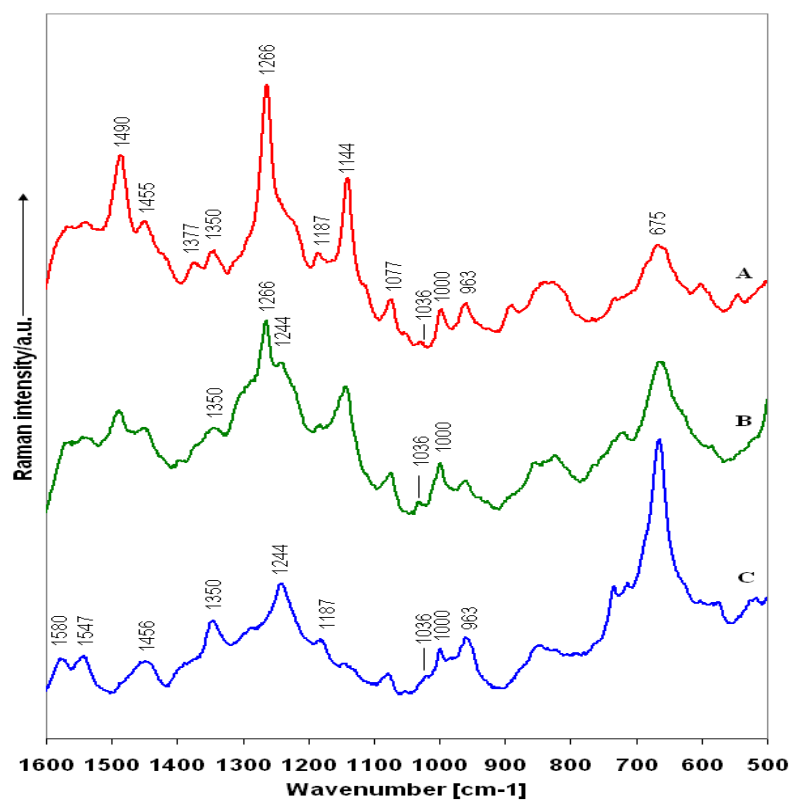


Fig. 25 SERS spectra of A $\beta$  after 24 hours in the nanochannel device. (A) 11.5pM (B) 1.15nM (C) 11.5Nm.

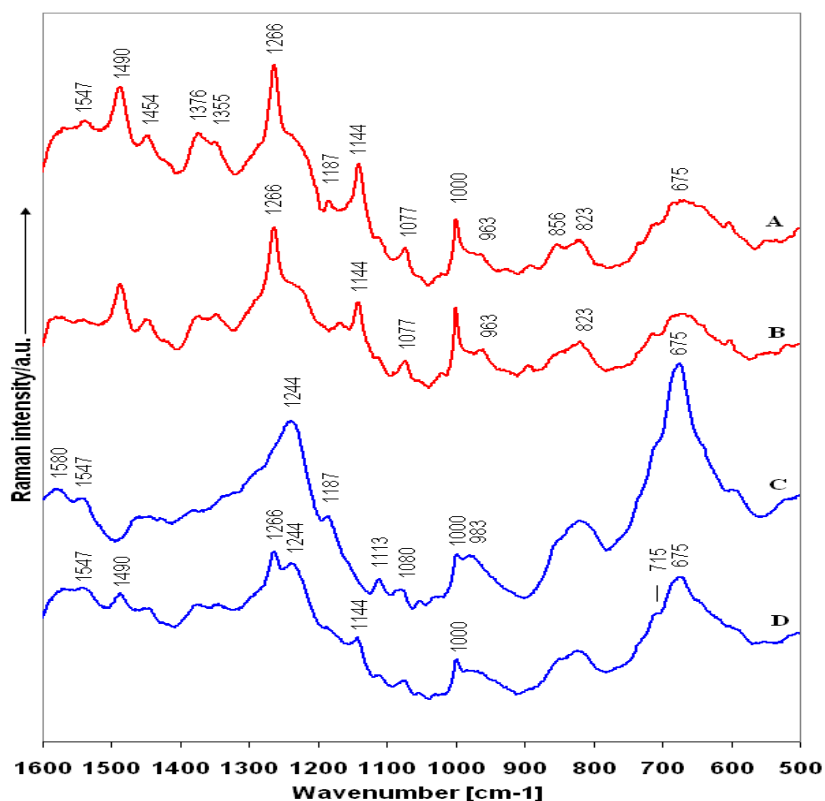


Fig. 26 SERS spectra of soluble A $\beta$  (1.15nM kept at 6 °C) after (A) 48 hours and (B) 38 hours in the nanochannel device. Insoluble A $\beta$  oligomer (1.15 nM at room temperature) after (C) 48 hours and (D) 38 hours.

Compared to other SERS techniques, this nanochannel device is favorable for A $\beta$  detection for several reasons: (1) The SERS active environment is highly reproducible since nanoparticle-molecule clusters are always aggregated at the same, specific location, namely, the entrance to the nanochannel. (2) The device has a higher sensitivity than other SERS substrates because the target molecules become more concentrated over time at the entrance to the nanochannel. (3) The bioactivity of A $\beta$  is preserved, allowing the protein to undergo conformational changes. Therefore, we can probe proteins in solution without modifying the protein, implying direct detection of A $\beta$  in cerebrospinal fluid.

Furthermore, the system's sensitivity to distinguishing between  $\alpha$ -helices and  $\beta$ -sheets as well as other protein conformational changes facilitates the discrimination between harmless monomeric forms of A $\beta$  and more toxic  $\beta$ -sheet oligomeric or protofibril/fibril forms. Tools such as the nanochannel device described here may be valuable in the detection and structure determination of A $\beta$  associated with the progression of Alzheimer's disease.

#### 4.6.2 Detection of the Conformational Change of Protein

To further explore the applications of this nanochannel, we used this device to probe the spectra of two proteins, insulin from bovine pancreas and bovine serum albumin (BSA), at room temperature (RT) and elevated temperatures, to investigate the ability to detect denaturation of protein due to the heat. During heat denaturation, the secondary structure of proteins changes and the proteins unfold from their original form. Insulin and BSA were both purchased from Sigma Aldrich. Insulin was in solution with a concentration of 10 mg/mL in 25 mM HEPES (pH 8.2) and BSA was in powder form. Before the experiment, the proteins were stored at 6 °C. The proteins were also diluted with DI water to 10 ng/L. During the experiments, a heated water bath was used to denature the proteins. Three samples of each protein were prepared. One was mixed with gold nanoparticles at room temperature without heating. The other two were placed into a heated bath at 60 °C and 100 °C for 10 minutes, respectively, right before they were mixed with gold nanoparticles. Gold nanoparticles suspended in water were purchased from Polysciences Inc. The volume ratio of protein solution and gold nanoparticles was



1:10. This mixing diluted the sample concentration further to 0.9 ng/L for both proteins. Immediately after mixing, six samples (BSA at room temperature, BSA heated to 60°C, BSA heated to 100°C, Insulin at room temperature, Insulin at 60°C, and Insulin at 100°C) with a volume of 5  $\mu$ L were dispensed into the inlet reservoirs of six independent nanochannel channels. Within three minutes the aggregation of gold nanoparticles became visible under the microscope and SERS spectra were collected. The SERS data were collected using a HORIBA Jobin Yvon LabRam IR/Raman system with a 785 nm laser excitation. A 50x objective (NA = 0.45) lens was used to focus the light onto the gold clusters. The laser power on the sample was 70  $\mu$ W. The scanning range was from 600  $\text{cm}^{-1}$  ~1600  $\text{cm}^{-1}$  with an integration time of 60 seconds. Five spectra were collected from three samples for each protein, then normalized and averaged to get the final spectra profile. The spectra shown in Fig. 27 and Fig. 28 under different conditions were offset for visual clarity. The assignment of peaks shown in Table 1 and Table 2 were made as determined from the literature.<sup>217-222</sup>

The characteristic peaks for insulin and BSA at an ultra-low concentration are clearly identified by using the nanochannel channel and SERS detection. More importantly, the information of the change of structures at different temperatures is also provided.

BSA is a globular protein, composed at room temperature primarily of  $\alpha$ -helices and random coils.<sup>223,224</sup> With our nanochannel device, detection of BSA at 0.9 ng/L was achieved successfully. The averaged normalized spectra at different temperatures are shown in Fig. 27. The assignment of peaks for spectrum A, which is the BSA without

heat, can be found in Table 1. From these three spectra, we can tell that as the temperatures increases, the structure of BSA is denatured. There is an intense band at  $1277\text{ cm}^{-1}$ , indicating strong  $\alpha$ -helical secondary structure. The intensity of this band decreases appreciably for samples heated at elevated temperatures, which indicates a loss in secondary structure and supports unfolding of the protein. For the sample heated at  $60\text{ }^{\circ}\text{C}$ , this band, although still intense, broadens and shifts to the right. For the  $100\text{ }^{\circ}\text{C}$  sample, a small shoulder develops at  $1296\text{ cm}^{-1}$ , indicative of  $\beta$ -sheet structure,<sup>221</sup> which supports that some  $\beta$ -sheet structures may be formed upon thermal denaturation.<sup>223,224</sup>

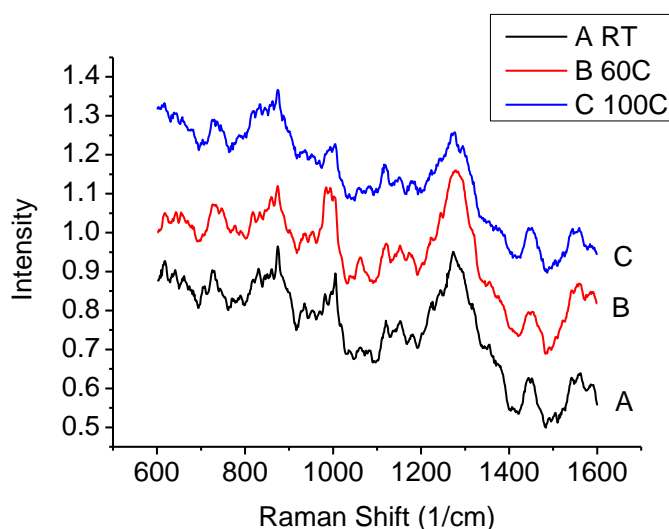


Fig. 27 SERS spectra of BSA at different temperatures (RT,  $60^{\circ}\text{C}$ ,  $100^{\circ}\text{C}$ ).

Table 1 Assignment of peaks in BSA spectrum (RT)

<i>wavenumber</i>	<i>Assignment</i>	
620	COO <sup>-</sup> wag or Phenylalanine	
643	ring deformation	Tyr
662	C-S stretching vibration	Cys
730	COO <sup>-</sup> def	backbone
832	Stretching and ring breathing mode	Tyr
876	indole ring	Trp
938	$\alpha$ -helical C-C stretch	
957	C-C stretch	
993	indole assymetric breath	Trp
1007	Strong, "breathing" vibration of the benzene ring	Phe
1184		Phe, Tyr
1233	$\beta$ -sheet (amide III region)	
1254	Random coil (amide III region)	
1277	$\alpha$ -helix (amide III region)	
1356	indole vibration	Trp
1453	CH <sub>2</sub> bending/scissoring mode	
1564	amide II band	
1593	COO <sup>-</sup> asymmetric stretch	backbone

The medium band at 938 cm<sup>-1</sup> is tentatively assigned to skeletal C-C stretching vibration characteristic of  $\alpha$ -helical conformation. This band decreases by about 25% in the 60 °C spectra, and then by 50% in the 100 °C, indicating a incomplete loss in  $\alpha$ -helical content.<sup>221</sup> Furthermore, the amide III band indicative of high  $\alpha$ -helical content, still existed at the elevated temperature, although with a decreased intensity. Thus, it appears that 10 minute heating at 60 °C/100 °C did not completely denature the secondary structure of protein. Further, the 1007 cm<sup>-1</sup> line, tentatively assigned to the breathing vibration of the benzene ring of phenylalanine, also decreases with temperature. This may be due to the unfolding of the protein in which the phenylalanine residue is not close to the gold nanoparticle. Moreover, the low intensity of this

stretching vibration suggests that the phenylalanine residues are not close to the gold surface or adopt a parallel orientation relative to the surface.<sup>219</sup>

In addition, the band at  $1453\text{ cm}^{-1}$  remains relatively the same, indicating that this methylene bending vibration is not sensitive to structure change.<sup>221</sup> On the other hand, the  $662\text{ cm}^{-1}$  band shifts to  $659\text{ cm}^{-1}$  for the sample heated to  $60\text{ }^{\circ}\text{C}$  and then to  $657\text{ cm}^{-1}$  for  $100^{\circ}\text{C}$ . This is likely due to the rearrangement of the conformation of the disulfide bonds in BSA.

Insulin is also a globular protein, composed of two polypeptides (the  $\alpha$ - and  $\beta$ -chain) joined by disulfide bonds, both exhibiting  $\alpha$ -helical and random coil conformation.<sup>225</sup> The spectra taken at different temperatures for insulin are shown in Fig. 28. The assignment of peaks for spectrum A, which is insulin before being heated, can be found in Table 2. Similar to BSA, its secondary structure was changed but not completely destroyed by the heat. The sharp peak at  $1276\text{ cm}^{-1}$  lies in the amide III region, which represents the N-H in- plane bending mode of the peptide bond.<sup>218,222, 226</sup> Upon denaturation, the band decreases considerably and broadens into a shoulder. It is proposed that the insulin conformation exhibits some  $\beta$ -sheet conformation upon thermal denaturation,<sup>222</sup> which is supported by the broadening of the band to include the  $1245\text{ cm}^{-1}$  region at  $100\text{ }^{\circ}\text{C}$ . This band is tentatively assigned to  $\beta$ -sheet and/or random coil conformation.<sup>218,222, 226</sup>

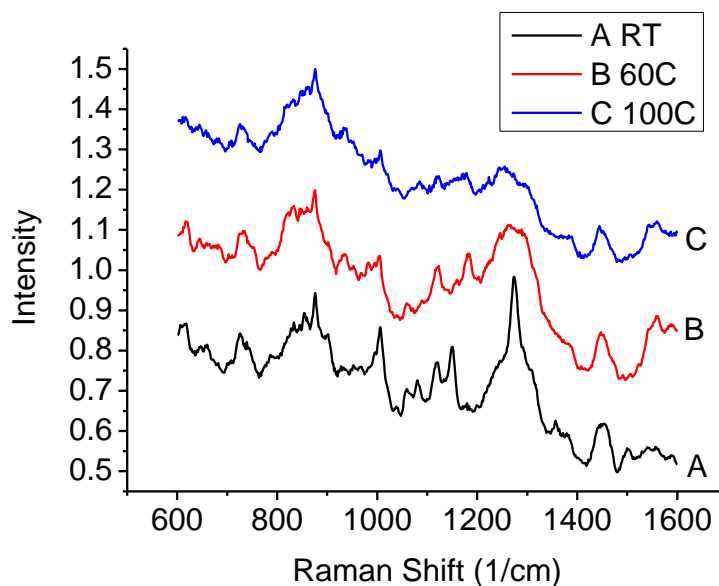


Fig. 28 SERS spectra of insulin at different temperatures (RT, 60°C, 100°C).

Table 2 Assignment of peaks in insulin spectrum (RT)

<i>wavenumber</i>	<i>Assignment</i>	
620	COO <sup>-</sup> wag or Phenylalanine	
662	C-S Stretching vibration	Cys
835	Stretching and ring breathing mode,	Tyr doublet
855	Stretching and ring breathing mode	Tyr doublet
938	$\alpha$ -helical C-C stretching vibration	
963	C-COO <sup>-</sup> stretch	
1007	Stretching and benzyl ring breathing mode	Phe
1050	$\beta$ -sheet (amide III region)	
1066	C-N stretch	
1081	C-N stretch	
1121	NH <sub>3</sub> <sup>+</sup> deformation	
1151	NH <sub>3</sub> <sup>+</sup> deformation	
1276	$\alpha$ -helix (amide III region)	
1311	CH <sub>2</sub> wag	
1457	CH <sub>2</sub> scissoring or bending mode	
1552	Amide II band	
1564	Amide II band	
1594	COO <sup>-</sup> assymmetric stretch	backbone

The  $640\text{ cm}^{-1}$  -  $680\text{ cm}^{-1}$  region is a mixed vibration area, the small shifts, appearance, and disappearance of bands could also be attributed to conformational changes in the disulfide bonds of the cysteine residues as also seen in the BSA spectra. The drastic change in the  $1050\text{ cm}^{-1}$  -  $1200\text{ cm}^{-1}$  region indicates an extreme unfolding of the protein backbone. The two small resolved peaks at  $1066\text{ cm}^{-1}$  and  $1081\text{ cm}^{-1}$  (tentatively assigned to the stretching vibration of C-N) also disappear at  $100\text{ }^{\circ}\text{C}$ . The weak, resolved bands attributed to the C-N modes indicate that these bonds are in close proximity and likely parallel to the gold surface; however, they are not directly adsorbed to the surface.

An interesting feature lies in the tyrosine residues - a doublet appears at  $835\text{ cm}^{-1}$  and  $855\text{ cm}^{-1}$ . This doublet is sensitive to changes in the local environment, manifested when the ratios of the two bands differ. As can be seen from the activity in the region, denaturation of the protein likely alters the degree to which the tyrosine residues are exposed to aqueous solution and to the gold nanoparticle surface, providing further evidence that the protein is denatured.<sup>219,222,226</sup> Plus, at  $620\text{ cm}^{-1}$  and  $1005\text{ cm}^{-1}$ , the phenylalanine ring breathing mode is resolved at room temperature and disappears upon heating to  $100\text{ }^{\circ}\text{C}$ .<sup>219,222,226</sup>

Small bands from  $1500\text{ cm}^{-1}$  -  $1580\text{ cm}^{-1}$  in the insulin spectra are resolved at room temperature. This region represents the amide II band ( $1520\text{ cm}^{-1}$  -  $1540\text{ cm}^{-1}$  or  $1555\text{ cm}^{-1}$  -  $1560\text{ cm}^{-1}$ ) and modes assigned to asymmetric carboxylate stretching vibrations, histidine and/or phenylalanine. Heating the protein to  $60\text{ }^{\circ}\text{C}$ , the amide II bands disappear, and the shoulder centered at  $1560\text{ cm}^{-1}$  and  $1585\text{ cm}^{-1}$ , becomes more

resolved and heightens in intensity, implying the carboxylate and histidine and/or phenylalanine are in close proximity to the gold surface.<sup>227</sup> In the spectra taken at 100 °C, the bands that were enhanced have decreased in intensity, with the 1585 cm<sup>-1</sup> band disappearing altogether. Furthermore, The proteins likely interact with the gold surface via its carboxyl groups of aspartic and glutamic acid and the C-terminus, as evidenced by the carboxylate stretching, deformation, and wagging vibrations (tentatively assigned to 965 cm<sup>-1</sup>, 730 cm<sup>-1</sup> and 620 cm<sup>-1</sup> respectively), and/or via the aromatic residues due to the previously mentioned spectral shifts, reflecting different orientation or geometry of the amino acid residues.<sup>217-222</sup>

From the previous discussion, we can conclude that insulin and BSA show conformational changes from  $\alpha$ -helix to  $\beta$ -sheet with increased heat as confirmed by monitoring the SERS spectra with the aid of nanochannel device. This nanochannel device can potentially be used to identify abnormal proteins with  $\beta$ -sheet conformation, which are associated with many human diseases.

#### 4.6.3 Other Applications

Currently, the research of using this device to identify cardiac biomarkers is going on. It has successfully detected cardiac biomarkers such as b-type natriuretic peptide (BNP), C-reactive protein (CRP), and cardiac troponin (cTn).<sup>228</sup> Cardiac biomarkers can provide early identification and diagnosis of acute coronary syndrome, and can provide information on the prognosis of the patient. In addition, the biomarkers can serve as criteria for admission, indicate possibility of re-infarction, or eliminate

coronary artery disease as a diagnosis altogether. Future work will focus on development and optimization of an assay to provide quantitative information.

This device has also detected estrogen at a concentration in nanogram per liter range. Another possible application associated with this preliminary result is the environmental hormone or toxin detection/monitoring in water.

From the discussion in section 4, we can summarize the advantages of this nanochannel device: (1) It can improve the detection sensitivity significantly because of an increased local density of nanoparticle/target molecules. (2) It can provide efficient and reproducible detection. With a condense hot spot produced at the nanochannel entrance, the detection area can be visually identified fast without randomly searching for hot spot. The detection is usually finished within minutes after sample loading.(3) This device does not require chemical agents or salts to initiate the aggregation of nanoparticles, which can preserve the original form of samples sensitive to chemical agents or salts. (4) The device can be fabricated on fused silica or borosilicate wafers at a low-cost using standard photolithography. Mass-production is feasible. The on-chip property also enables the capability of parallel analysis. (5)The sample consumption of this device is extremely low, which is preferred for expensive or mass-limited samples. One micro-liter sample is enough in practical detection.



## 5. SUMMARY

In this dissertation, three nanochannel devices used for different applications were demonstrated. An overview of fabrication techniques was given as an introduction to nanochannel fabrication. Then three different fabrication techniques were discussed in details for fabricating the nanochannel devices.

(1) An innovative scanning coaxial electrospinning process was developed for nanochannel device used in single molecule detection. As a bottom-up technique, this process can produce nanochannel with a high throughput and low cost. Silica nanochannels with a circular opening as small as 15 nm were formed. The influences of various fabrication process parameters were discussed.

To demonstrate the merits of using nanochannel for single molecule detection, photon bursts originating from fluorescent dyes (IAF) moving through nanochannel has been reported. With a 15nm inner diameter, the nanochannel device confined a detection volume in zeptoliter range and detected single dyes in an environment of high sample concentration ( $\mu\text{M}$ ). This is advantageous to identify an extremely low concentration of target molecules amid a high concentration of background sample.

(2) A heat-induced stretching approach was developed to fabricate nanochannels with a circular opening from micrometer-sized fused silica capillary tubing. This is a straightforward top-down fabrication technique. From a capillary tubing with an inner diameter of 2  $\mu\text{m}$ , a nanochannel with 200 nm can be formed under thermal deformation and stretching. The main challenge of this fabrication approach is that the inner diameter of resultant channels is not uniform along the entire length. Because of the limitation of

experiment facilities, the whole experiment set-up is a simple and crude initial prototype although demonstrating the capability of producing nanochannels. A more precise-controlled mechanical system should be able to improve the understanding and performance of this approach, based on which a synthetic theoretical analysis could also be established.

To demonstrate the application of nanochannel for electrokinetic analysis, IAF solution was introduced into the channel. Photon bursts originating from IAF molecules moving through the nanochannel under different electrical potential were monitored. From the photon burst counts, it can be concluded that the molecule transport in the nanochannel is enhanced under electrokinetic potential. The potential application of these nanochannels is used together with single molecule to identify extremely low concentration of target molecules among a high concentration of background analyte, which is particularly appealing in diagnostic applications, such as the detection of tumor markers in human body fluid for early cancer diagnosis.

(3) A nanochannel trapping device with a step structure was designed and developed. It highly improves the detection efficiency, consistency and sensitivity of SERS detection and provides characteristic structural information of aqueous samples at ultra-low concentration (e.g. in pico molar range) within minutes. This part of research is the most important work during my PhD study. This nanochannel was fabricated using standard contact lithography followed by wet/dry etching and thermal bonding. Multiple nanochannels can be fabricated on a single wafer. More specifically, 16 nanochannels was fabricated on one 4" wafer, which enables parallel analysis.

With a pinched micro-nanochannel structure, consistent aggregation of SERS-active nanostructures, namely, gold nanoparticles, was formed at a predictable location. This aggregation of condense hot spot and molecule enrichment effect enables the significant improve in detection sensitivity of SERS. This device detected adenine at a concentration as low as 10 pM. Moreover, it also detected multiple analytes in aqueous solution simultaneously with adenine and congo red as the sample. The nanochannel was further used to detect the biomarker for Alzheimer's disease - A $\beta$ , at ultra-low concentration (nM and pM). From the SERS spectra, A $\beta$  in different conformational states during its self -assembly process was observed. This result could have a large impact on the understanding and diagnosing of Alzheimer's disease.

The nanochannel was used to identify the denaturation of proteins with insulin and BSA as samples. The secondary structural information of proteins was extracted from the SERS data. This nanochannel also has potential applications in the detection of water contaminants and diagnosis of acute coronary syndrome.

These nanochannels have shown their unique advantages in bio/chemical analysis. However, the fabrication is still the bottle-neck in the development of nanochannel devices. The fabrication approaches described here also have their limitations and challenges. The nanochannel fabricated from electrospinning process has a variation of size among collected samples. This might be due to the random enviroment interruptions, such as air flow or the inconsistency of mechanical pumping. Although there is a mechanism explanation developed for electrospinning, an accurate theoretical analysis and modeling is still challenging. This is the same

situation for heat-induced stretching approach. This dissertation focuses on the experimental results rather than theoretical analysis. Future work might include the qualitative understanding and analysis of the mechanism for these approaches.

For the nanochannel trapping device, photolithography-based fabrication was used. Comparing to the other two fabrication methods, this fabrication process is much more mature and able to be precisely controlled. The key challenge in this process is the bonding step. Because of using PECVD A-Si as the etching mask, tiny particles were deposited on the wafer during the PECVD process. This results in a unsmooth surface of the wafer even after removing the A-Si layer and affects the bonding of two wafers. By changing the HF wet etching to reactive ion etching, the PECVD step can be avoided since photoresist can be used as the etching mask. However, in this way, the depth of microchannel would be limited to be 1~2  $\mu\text{m}$  due to the low selectivity of reactive ion etching ( $\text{CF}_4$  or  $\text{CHF}_3/\text{O}_2$ ) between photoresist and  $\text{SiO}_2$ . This depth would be enough for current applications. But it could be a problem if future applications include testing analytes with a size larger than 2  $\mu\text{m}$ .

Besides the fabrication, future work may also include the design of nanochannels. For the nanochannel trapping device, an associated channel system could be designed and incorporated with current device to integrate the sample preparation, separation, detection and waste collection on one single chip. The unnecessary cells/proteins could be eliminated in the separation channels and the analytes of interest could reach the detection channel. At last, the waste could be collected in the collection channels. The final goal would be developing a disposable

nanochannel system that is capable to identify analytes after a simple loading of sample (e.g. blood or human body fluids), for disease diagnosis or other applications.

## REFERENCES

1. J. O. Tegenfeldt, C. Prinz, H. Cao, R. L. Huang, R. H. Austin, S. Y. Chou, E. C. Cox, and J. C. Sturm, *Anal. Bioanal. Chem.*, 2004, **378**, 1678.
2. P. A. Auroux, D. Iossifidis, D. R. Reyes, and A. Manz, *Anal. Chem.*, 2002, **74**, 2637.
3. M. Foquet, J. Korlach, W. R. Zipfel, W. W. Webb, and H. G. Craighead, *Anal. Chem.*, 2004, **76**, 1618.
4. A. Rasmussen, M. Gaitan, L. E. Locascio and M. E. Zaghoul, *J. Microelectromech. Syst.*, 2001, **10**, 286.
5. D. Mijatovic, J. C. T. Eijkel and A. v. d. Berg, *Lab Chip*, 2005, **5**, 492.
6. J. Haneveld, H. Jansen, E. Berenschot, N. Tas and M. Elwenspoek, *J. Micromech. Microengin.*, 2003, **13**, S62.
7. E. D. Fabrizio, R. Fillipo, S. Cabrini, R. Kumar, F. Perennes, M. Altissimo, L. Businaro, D. Cojac, L. Vaccari, M. Prasciolu and P. Candeloro1, *J. Phys.: Condens. Matter*, 2004, **16**, S3517.
8. K. K. Matsumoto, M. Nakao, Y. Hatamura, T. Kitamori and T. Sawada, *Proc. IEEE MEMS*, 1998, 127.
9. C. K. Harnett, G. W. Coates and H. G. Craighead, *J. Vac. Sci. Technol. B.*, 2001, **19**, 2842.
10. K. A. Mahabadi, I. Rodriguez, S. C. Haur, J. A. v. Kan, A. A. Bettioli and F. Watt, *J. Micromech. Microeng.*, 2006, **16**, 1170.

11. D. M. Cannon, B. R. Flachsbart, M. A. Shannon and J. V. Sweedler, *Appl. Phys. Lett.*, 2004, **85**, 1241.
12. S. Arscott and D. Troadec, *Nanotechnology*, 2005, **16**, 2295.
13. M. J. O'Brien, P. Bisong, L. K. Ista, E. M. Rabinovich, A. L. Garcia, S. S. Sibbett, G. P. Lopez and S. R. J. Brueck, *J. Vac. Sci. Technol. B.*, 2003, **21**, 2941.
14. H. Cao, Z. Yu, J. Wang, J. O. Tegenfeldt, R. H. Austin, E. Chen, W. Wu and S. Y. Chou, *Appl. Phys. Lett.*, 2002, **81**, 174.
15. L. J. Guo, X. Cheng and C. Chou, *Nano Lett.*, 2003, **4**, 69.
16. H. H. Solak, C. David, J. Gobrecht, L. Wang and F. Cerrina, *J. Vac. Sci. & Tech. B*, 2002, **20**, 2844.
17. S. H. Zaidi and S. R. J. Brueck, *J. Vac. Sci. & Tech. B*, 1993, **11**, 658.
18. M. Wang, N. Jing, I.-H. Chou, G. L. Cote and J. Kameoka, *Lab Chip*, 2007, **7**, 630.
19. J. Han and H. G. Craighead, *J. Vac. Sci. Tech. A*, 1999, **17**, 2142.
20. W. Li, J. O. Tegenfeldt, L. Chen, R. H. Austin, S. Y. Chou, P. A. Kohl, J. Krotine and J. C. Sturm, *Nanotechnology*, 2003, **14**, 578.
21. R. Ramaseshan, S. Sundarrajan, R. Jose and S. Ramakrishna, *J. Appl. Phys.*, 2007, **102**, 111101.
22. D. Li, J. T. McCann and Y. Xia, *J. Am. Ceram. Soc.*, 2006, **89**, 1861.
23. M. Foquet, J. Korlach, W. Zipfel, W. W. Webb and H. G. Craighead, *Anal. Chem.*, 2002, **74**, 1415.

24. M. Foquet, J. Korlach, W. R. Zipfel, W. W. Webb and H. G. Craighead, *Anal. Chem.*, 2004, **76**, 1618.
25. S. M. Stavis, J. B. Edel, K. T. Samiee and H. G. Craighead, *Lab Chip*, 2005, **5**, 337.
26. B. Valeur, *Molecular Fluorescence*, Wiley-VCH, Weinheim, Germany, 2002.
27. S. R. Aragon and R. Pecora, *Biopolymer*, 1975, **14**, 119.
28. J. P. Bouchaud and A. Georges, *Phys. Rep.*, 1990, **195**, 127.
29. W. Denk, J. J. Strickler and W. W. Webb, *Science*, 1990, **248**, 73.
30. L. Edman, U. Mets and R. Rigler, *Proc. Nat. Accd. Sci. USA*, 1996, **93**, 6710.
31. M. Ehrenberg and R. Rigler, *Chem. Phy.*, 1974, **4**, 390.
32. M. Ehrenberg and R. Rigler, *Quart. Rev. Biophys.*, 1976, **9**, 69.
33. M. Brinkmeir, K. Dorre, J. Stephan and M. Eigen, *Anal. Chem.*, 1999, **71**, 609.
34. Y. Chen, J. D. Muller, S. Y. Tetin, J. D. Tyner and E. Gratton, *Biophys. J.*, 2000, **79**, 1074.
35. P. Dittrich, F. Campeggi, M. Jahnz and P. Schwile, *Biol. Chem*, 2000, **382**, 491.
36. C. Eggeling, J. R. Fries, L. Brand and C. A. M. Seidel, *Proc. Nat. Accd. Sci. USA*, 1998, **95**, 1556.
37. M. Eigen and R. Rigler, *Proc. Nat. Accd. Sci. USA*, 1994, **91**, 5740.
38. E. L. Elson and D. Magde, *Biopolymers*, 1974, **13**, 1.
39. A. Gennerich and D. Schild, *Biophys. J.*, 2000, **79**, 3294.
40. U. Haupts, S. Maiti, P. Scheille and W. W. Web, *Proc. Nat. Accd. Sci. USA*, 1998, **95**, 13573.



41. K. G. Heinze, A. Kolterman and P. Schwille, *Proc. Nat. Accd. Sci. USA*, 2000, **97**, 10377.
42. P. Kask, P. Piksarv, U. Mets and E. Lippma, *Eur. Biophys. J.*, 1987, **14**, 257.
43. M. Kinjo and R. Rigler, *Nucleic Acids Res.*, 1995, **23**, 1795.
44. J. Korlach, P. Schwille and W. W. Webb, *Proc. Nat. Accd. Sci. USA*, 1999, **95**, 1421.
45. U. Kettling, A. Kolterman, P. Schwille and M. Eigen, *Proc. Nat. Accd. Sci. USA*, 1998, **95**, 14116.
46. D. Magde, E. L. Elson and W. W. Webb, *Biopolymers*, 1974, **13**, 29.
47. M. J. Levene, J. Korlach, S. W. Turner, M. Foquet, H. G. Craighead and W. W. Webb, *Science*, 2003, **299**, 682.
48. L. Sacconi, D. A. Dombek and W. W. Webb, *PNAS*, 2006, **103**, 3124.
49. P. Schwille, S. Kummer, A. A. Heikal, W. E. Moerner and W. W. Webb, *PNAS*, 2000, **97**, 151.
50. S. T. Hess, S. Huang, A. A. Heikal and W. W. Webb, *Biochemistry*, 2002, **41**.
51. J. Khandurina, S. C. Jacobson, L. C. Waters, R. S. Foote and J. M. Ramsey, *Anal. Chem.*, 1999, **71**, 1815.
52. E. T. Lagally, P. C. Simpson and R. A. Mathies, *Sens. Actuators B*, 2000, **63**, 138.
53. M. Foquet, J. Korlach, W. Zipfel, W. W. Webb and H. G. Craighead, *Anal. Chem.*, 2002, **74**, 1415.
54. M. Foquet, J. Korlach, W. R. Zipfel, W. W. Webb and H. G. Craighead, *Anal. Chem.*, 2004, **76**, 1618.

55. C. Y. Kung, M. D. Barnes, N. Lermer, W. B. Whitten and J. M. Ramsey, *Anal. Chem.*, 1998, **70**, 658.
56. R. Qiao and N. R. Aluru, *Appl. Phys. Lett.*, 2005, **86**, 143105.
57. C. W. Hollars and J. Puls, *Anal. Bioanal. Chem.*, 2006, **385**, 1384.
58. M. A. Stavis and J. B. Edel, *Lab Chip*, 2005, **5**, 337.
59. D. Li and Y. Xia, *Nano Lett.*, 2004, **4**, 933.
60. I. G. Loscertales, A. Barrero, M. Marquez, R. Spretz, R. Velarde-Ortiz, and G. Larsen, *J. Am. Chem. Soc.*, 2004, **126**, 5376.
61. A. Formhals, 1975504, US Patent, 1934.
62. D. Li and Y. Xia, *Adv. Mater.*, 2004, **16**, 1151.
63. S.-S. Choi, Y. S. Lee, C. W. Joo, S. G. Lee, J. K. Park and K.-S. Han, *Electrochimica Acta.*, 2004, **50**, 339.
64. S. W. Choi, S. M. Jo, W. S. Lee and Y. R. Kim, *Adv. Mater.*, 2003, **15**, 2027.
65. K. H. Lee, H. Y. Kim, M. S. Khil, Y. M. Ra and D. R. Lee, *Polymer*, 2003, **44**, 1287.
66. S. A. Theron, E. Zussman and A. L. Yarin, *Polymer*, 2004, **45**, 2017.
67. Y. You, B.-M. Min, S. J. Lee, T. S. Lee and W. H. Park, *J. Appl. Polymer Sci.*, 2004, **95**, 193
68. C. L. Casper, J. S. Stephens, N. G. Tassi, D. B. Chase and J. F. Rabolt, *Macromolecules*, 2004, **37**, 573.
69. J. Kameoka, S. S. Verbridge, H. Liu, D. A. Czaplewski and H. G. Craighead, *Nano Lett.*, 2004, **4**, 2105.

70. D. Li, T. Herricks and Y. Xia, *Appl. Phys. Lett.*, 2003, **83**, 4586.
71. D. Li, Y. Wang and Y. Xia, *Nano Lett.*, 2003, **3**, 1167.
72. D. Li, Y. Wang and Y. Xia, *Adv. Mater.*, 2004, **16**, 361.
73. A. Theron, E. Zussman and A. L. Yarin, *Nanotechnology*, 2001, **12**, 384.
74. J. Kameoka and H. G. Craighead, *Appl. Phys. Lett.*, 2003, **83**, 371.
75. J. Kameoka, R. Orth, Y. Yang, D. Czaplewski, R. Mathers, G. W. Coates and H. G. Craighead, *Nanotechnology*, 2003, **14**, 1124.
76. D. Li, A. Babel, S. A. Jenekhe and Y. Xia, *Adv. Mater.*, 2004, **16**, 2062.
77. Z. Sun, E. Zussman, A. L. Yarin, J. H. Wendorff and A. Greiner, *Adv. Mater.*, 2003, **15**, 1929.
78. J. H. Yu, S. V. Fridrikh and G. C. Rutledge, *Adv. Mater.*, 2004, **16**, 1562.
79. Y. Zhang, Z.-M. Huang, X. Xu, C. T. Lim and S. Ramakrishna, *Chem. Mater.*, 2004, **16**, 3406.
80. D. Li, J. T. McCann and Y. Xia, *Small*, 2005, **1**, 83.
81. J. T. McCann, D. Li and Y. Xia, *J. Mater. Chem.*, 2005, **15**, 735.
82. X. Wang, Y.-G. Kim, C. Drew, B.-C. Ku, J. Kumar and L. A. Samuelson, *Nano Lett.*, 2004, **4**, 331.
83. C. Drew, X. Liu, D. Ziegler, X. Wang, F. F. Bruno, J. Whitten, L. A. Samuelson and J. Kumar, *Nano Lett.*, 2003, **3**, 143.
84. G.-M. Kim, A. Wutzler, H.-J. Radusch, G. H. Michler, P. Simon, R. A. Sperling and W. J. Parak, *Chem. Mater.*, 2005, **17**, 4949.

85. A. C. Patel, S. Li, C. Wang, W. Zhang and Y. Wei, *Chem. Mater.*, 2007, **19**, 1231.
86. A. Greiner and J. H. Wendorff, *Angew. Chem. Int. Ed.*, 2007, **46**, 5670.
87. T. Subbiah, G. S. Bhat, R. W. Tock, S. Parameswaran and S. S. Ramkumar, *J. Appl. Polym. Sci.*, 2005, **96**, 557.
88. M. M. Hohman, M. Shin, G. Rutledge and M. P. Brenner, *Phys. Fluids*, 2001, **13**, 2201.
89. M. M. Hohman, M. Shin, G. Rutledge and M. P. Brenner, *Phys. Fluids*, 2001, **13**, 2221.
90. Y. M. Shin, M. M. Hohman, M. P. Brenner and G. C. Rutledge, *Polymer*, 2001, **42**, 9955.
91. A. L. Yarin, S. Koombhongse and D. H. Reneker, *J. Appl. Phys.*, 2001, **90**, 4836.
92. M. Bognitzki, H. Hou, M. Ishaque, T. Frese, M. Hellwig, C. Schwarte, A. Schaper, J. H. Wendorff and A. Greiner, *Adv. Mater.*, 2000, **12**, 637.
93. R. A. Caruso, J. H. Schattka and A. Greiner, *Adv. Mater.*, 2001, **13**, 1577.
94. D. A. Czaplewski, J. Kameoka, R. Mathers, G. W. Coates and H. G. Craighead, *Appl. Phys. Lett.*, 2003, **83**, 4836.
95. H. Dong, S. Prasad, V. Nyame and W. E. Jones, *Chem. Mater.*, 2004, **16**, 371.
96. H. Hou, Z. Jun, A. Reuning, A. Schaper, J. H. Wendorff and A. Greiner, *Macromolecules*, 2002, **35**, 2429.
97. M. Wang, N. Jing, C. B. Su, J. Kameoka, C.-K. Chou, M.-C. Hung and K.-A. Chang, *Appl. Phys. Lett.*, 2006, **88**, 033106.

98. H. Huang, R. M. Miura, W. P. Ireland and E. Puil, *SIAM J. Appl. Math.*, 2003, **63**, 1499.
99. X. Feng, A. K. Mairaj, D. W. Hewak and T. M. Monro, *J. Lightwave Tech.*, 2005, **23**, 2046.
100. K. Kneipp, H. Kneipp, I. Itzkan, R. R. Dasari and M. S. Feld, *J. Phys: Condens. Matter.*, 2002, **14**, R597.
101. M. Fleischman, P.J. Hendra and A. J. McQuillan, *Chem. Phys. Lett.*, 1974, **26**, 163
102. D.J. Jeanmaire and R.P. VanDuyne, *J. Electroanal. Chem.*, 1977, **84**, 1.
103. M.G. Albrecht and J. A. Creighton, *J. Am. Chem. Soc.*, 1977, **99**, 5215.
104. H. J. Seki, *J. Electron Spectrosc. Relat. Phenom.*, 1986, **39**, 239.
105. M. Cardona and G. Guntherodt, *Light Scattering in Solids IV*. Springer, Berlin, Germany, 1984.
106. M. Moskovits, *Rev. Mod. Phys.*, 1985, **57**, 783.
107. A. Bachackashvili, S. Efrima, B. Katz and Z. Priel, *Chem. Phys. Lett.*, 1983, **94**, 571.
108. K. Kneipp, G. Hinzmann and D. Fassler, *Chem. Phys. Lett.*, 1983, **99**, 5.
109. P. Hildebrandt and M. Stockburger, *J. Phys. Chem.*, 1984, **88**, 5935.
110. B. Pettinger, *Chem. Phys. Lett.*, 1984, **110**, 576.
111. K. Kneipp, H. Kneipp and M. Rentsch, *J. Mol. Struct.*, 1987, **156**, 3.
112. B. Pettinger and K. Krischer, *J. Electron Spectrosc. Relat. Phenom.*, 1987, **45**,

113. K. Kneipp *Exp. Tech. Phys.*, 1988, **36**, 161
114. K. Kneipp, Y. Wang, H. Kneipp, L. T. Perelman, I. Itzkan, R. R. Dasari and M. S. Feld, *Phys. Rev. Lett.*, 1997, **78**, 1667
115. K. Kneipp, H. Kneipp, V. B. Kartha, R. Manoharan, G. Deinum, I. Itzkan, R. R. Dasari and M. S. Feld, *Phys. Rev. E*, 1998, **57**, R6281
116. J. D. Andrade, *Surface and Interfacial Aspects of Biomedical Polymers*, Plenum, New York, USA, 1985.
117. E. Koglin and J. M. Sequaris, *Top. Curr. Chem.*, 1986, **134**, 1
118. R. J. H. Clark and R. E. Hester, *Spectroscopy of Surfaces*, Wiley, Chichester, UK, 1988.
119. T. M. Cotton, Jae-Ho Kim and G. D. Chumanov, *J. Raman Spectrosc.*, 1991, **22**, 729
120. K. Sokolov, P. Khodorchenko, A. Petukhov, I. Nabiev, G. Chumanov and T. M. Cotton, *Appl. Spectrosc.*, 1993, **47**, 515
121. G.C. Schatz, *Acc. Chem. Res.*, 1984, **17**, 370
122. M. Kerker, *Acc. Chem. Res.*, 1984, **17**, 271
123. T. Vo-Dinh, *Chemical Analysis of Polycyclic Aromatic Compounds*, Wiley, New York, USA, 1989
124. H. D. Abruna, *In-situ Studies on Electrochemical Interfaces*, VCH Verlag Chemie, Berlin, Germany, 1991.
125. T. M. Cotton and E.S. Brandt, *Physical Methods of Chemistry*, Wiley, New York, USA, 1992.

126. A. Otto, I. Mrozek, H. Grabhorn and W. Akermann, *J. Phys. Condens. Matter.*, 1992, **4**, 1143.
127. P. Halevi, *Photonic Probes of Surfaces*, Elsevier, New York, USA, 1995.
128. J. J. Laserna, *Modern Techniques in Raman Spectroscopy*, Wiley, New York, USA, 1996.
129. R.K. Chang and T.E. Furtak, *Surface-Enhanced Raman Scattering*, Plenum, New York, USA, 1982.
130. P.A. Lund, R.R. Smardzewski and D.E. Terault, *Chem. Phys. Lett.*, 1982, **89**, 508.
131. B. H. Loo, *J. Chem. Phys.*, 1981, **75**, 5955.
132. T. H. Wood and M. V. Klein, *Solid State Commun.*, 1980, **35**, 263.
133. E. J. Zeman and G. C. Schatz, *J. Phys. Chem.*, 1987, **91**, 634.
134. H. Ehrenreich, F. Seitz and D. Turnbull, *Solid State Physics* edited, Academic Press, New York , USA, 1984.
135. I. Pockrand, *Surface-Enhanced Raman Vibrational Studies at Solid /Gas Interfaces*, Springer, Berlin, Germany, 1984.
136. P. Kambhampati, C. M. Child, M. C. Foster and A. Campion, *J. Chem. Phys.*, 1998, **108**, 5013.
137. M. Moskovits, *J. Raman Spectrosc.*, 2005, **36**, 485.
138. T. Vo-Dinh, *Trends Anal. Chem.*, 1998, **17**, 557.
139. H. Xu., J. Aizpurua, M. Käll and P. Apell, *Phys. Rev. E*, 2000, **62**, 4318.
140. M. Käll, H. Xu and P. Johansson, *J. Raman Spectrosc.*, 2005, **36**, 510.

141. J. R. Lombardi, R. L. Birke, T. Lu and J. Xu, *J. Chem. Phys.*, 1986, **84**, 8.
142. S. Nie and S. R. Emory, *Science*, 1997, **275**, 1102.
143. H. Wang, C. S. Levin. and N. J. Halas, *J. Am. Chem. Soc.*, 2005, **127**, 14992.
144. L. Gunnarsson, E. J. Bjerneld, H. Xu, S. Petronis, B. Kasemo and M. Käll, *Appl. Phys. Lett.*, 2001, **78**, 802.
145. N. Felidj, J. Aubard, G. Levi, J. R. Krenn, A. Hohenau, G. Schider, A. Leitner and F. R. Aussenegg, *Appl. Phys. Lett.*, 2003, **82**, 3095.
146. D. A. Genov, A. K. Sarychev, V. M. Shalaev and A. Wei, *Nano Lett.*, 2004, **4**, 153.
147. Y. Lu, G.. L. Liu. and L. P. Lee, *Nano Lett.*, 2005, **5**, 5.
148. F. Svedberg, Z. Li, H. Xu and M, Käll, *Nano Lett*, 2006, **6**, 2639.
149. J. E. Pemberton and R. P. Buck, *Anal. Chem.*, 1981, **53**, 2263.
150. B. Pettinger, U. Wenneng and H. Wetzels, *Surf. Sci.*, 1980, **101**, 409.
151. B. H. Loo, *J. Phys. Chem.*, 1983, **87**, 3003.
152. M. Fleishman, P. R. Graves and J. Robinson, *J. Electroanal. Chem.*, 1985, **182**, 87.
153. M. M. Carraba, R. B. Edmonds and R. D. Raugh, *Anal. Chem.*, 1987, **59**, 2559.
154. C. Jennings, R. Aroca, A. M. Hor and R. O. Loutfy, *Anal. Chem.*, 1984, **56**, 2033.
155. F. Ni, R. Sheng and T. M. Cotton, *Anal. Chem.*, 1990, **62**, 1958.
156. M. Meier, A. Wokaun and T. Vo-Dinh, *J. Phys. Chem.*, 1985, **89**, 1843.
157. T. Vo-Dinh, M. Meier and A. Wokaun, *Anal. Chim. Acta.*, 1986, **181**, 139.



158. R.Aroca and F.Martin, *J.Raman Spectrosc.*, 1986, **17**, 243.
159. G. D. Sockalingum, A. Beljebbar, H. Morjani, J. F. Angiboust and M. Manfait, *Biospectroscopy*, 1998, **4**, S71.
160. J. A. Creighton, C. G. Blatchford and M.G. Albrecht, *Faraday Trans.*, 1979, **75**,790.
161. P. C. Lee and D. Meisel, *J. Phys. Chem.*, 1982, **86**, 3391.
162. N. Leopold and B. Lendl, *J. Phys. Chem. B*, 2003, **107**, 5723.
163. N. Félidj, J. Aubard, G. Lévi, J. R. Krenn, M. Salerno, G. Schider, B. Lamprecht, A. Leitner, and F. R. Aussenegg, *Phys. Rev. B*, 2002, **65**, 075419-1.
164. N. Félidj, S. Lau Truong, J. Aubard, G. Lévi, J. R. Krenn, A. Hohenau, A. Leitner, and F. R. Aussenegg, *J. Chem. Phys.*, 2004, **120**, 7141.
165. N. Félidj, J. Aubard, G. Lévi, J. R. Krenn, A. Hohenau, G. Schider, A. Leitner, and F. R. Aussenegg, *Appl. Phys. Lett.*, 2003, **82**, 3095.
166. C. L. Haunes and R. P. Van Duyne, *Mater. Res. Soc. Symp. Proc.*, 2002, **728**, S10.7.1
167. T. R. Jensen, M. L. Duval, K. L. Kelly, A. A. Lazarides, G. C. Schatz and R. P. Van Duyne, *J. Phys. Chem. B*, 1999, **103**, 9846.
168. D. A. Weitz, S. Garoff and T. J. Gramila, *Opt. Lett.*, 1982, **7**, 168.
169. B. Nikoobakht and M. A. El-Sayed, *J. Phys. Chem. A*, 2003, **107**, 3372.
170. J. Fan, Y. Liu and Y. Zhao, *Nanoengineering: Fabrication, Properties, Optics, and Devices III*, Elizabeth A. Dobisz, Louay A. Eldada, Eds., *Proc. of SPIE*, 2006, **6327**, 63270R.

171. X. Hu, W. Cheng, T. Wang, Y. Wang, E. Wang and S. Dong, *J. Phys. Chem. B*, 2005, **109**, 19385.
172. Y. Joo and J. S. Suh, *Bull. Korean Chem. Soc.*, 1995, **16**, 808.
173. J. L. Yao, G. P. Pan, K. H. Xue, D. Y. Wu, B. Ren, D. M. Sun, J. Tang, X. Xu and Z. Q. Tian, *Pure Appl. Chem.*, 2000, **72**, 221.
174. S. B. Chaney, S. Shanmukh, R. A. Dluhy and Y. Zhao, *Appl. Phys. Lett.*, 2005, **87**, 031908.
175. B. Nikoobakht, J. Wang and M. A. El-Sayed, *Chem. Phys. Lett.*, 2002, **366**, 17.
176. S. Shanmukh, L. Jones, J. Driskell, Y. Zhao, R. Dluhy and R. A. Tripp, *Nano Lett.*, 2006, **6**, 2630.
177. C. Viets and W.J. Hill, *Raman Spectrosc.*, 2000, **31**, 625.
178. L. A. Dick, A. J. Haes and R. P. Van Duyne, *J. Phys. Chem. B*, 2000, **104**, 11752.
179. V. Deckert, D. Zeisel, R. Zenobi and T. Vo-Dinh, *Anal. Chem.*, 1998, **70**, 2646.
180. P. A. Schueler, J. T. Ives, F. DeLaCroix, W. B. Lacy, P. A. Becker, J. Li, K. D. Caldwell, B. Drake and J. M. Harris, *Anal. Chem.*, 1993, **65**, 3177.
181. M. Litorja, C. L. Haynes, A. J. Haes, T. R. Jensen and R. P. Van Duyne, *J. Phys. Chem. B*, 2001, **105**, 6907.
182. S. Kubo, Z. Gu, D. A. Tryk, Y. Ohko, O. Sato and A. Fujishima, *Langmuir*, 2002, **18**, 5043.
183. J. M. Bello, D. L. Stokes and T. Vo-Dinh, *Appl. Spectrosc.*, 1989, **43**, 1325.
184. T. Vo-Dinh, *Trends Anal. Chem.*, 1998, **17**, 557.

185. L. A. Dick, A. D. McFarland, C. L. Haynes and R. P. Van Duyne, *J. Phys. Chem. B*, 2002, **106**, 853.
186. S. J. Oldenburg, S. L. Westcott, R. D. Averitt and N. J. Halas, *J. Chem. Phys.*, 1999, **111**, 4729.
187. J. B. Jackson, S. L. Westcott, L. R. Hirsch, J. L. West and N. J. Halas, *Appl. Phys. Lett.*, 2003, **82**, 257.
188. J. B. Jackson and N. J. Halas, *Proc. Nat. Accd. Sci. USA*, 2004, **101**, 17930.
189. C. E. Talley, J. B. Jackson, C. Oubre, N. K. Grady, C. W. Hollars, S. M. Lane, T. R. Huser, P. Nordlander and N. J. Halas, *Nano. Lett.*, 2005, **5**, 1569.
190. N. R. Jana, *Analyst*, 2003, **128**, 954.
191. R. D. Averitt, D. Sarkar and N. J. Halas, *Phys. Rev. Lett.*, 1997, **78**, 4217.
192. S. J. Oldenburg, R. D. Averitt, S. L. Westcott and N. J. Halas, *Chem. Phys. Lett.*, 1998, **288**, 243.
193. G. Mie, *Ann. Phys.*, 1908, **24**, 377.
194. A. Taflove and S. C. Hagness, *Computational Electrodynamics*, Artech House, Boston, USA, 2000.
195. D. L. Stokes and T. Vo-Dinh, *Sens. Actuators B*, 2000, **69**, 28.
196. M. S. Anderson, *Appl. Phys. Lett.*, 2000, **76**, 3130.
197. R. M. Stockle, S. Yung Doug, V. Deckert and R. Zenobi, *Chem. Phys. Lett.*, 2000, **318**, 131.
198. B. Pettinger, G. Picardi, R. Schuster and G. Ertl, *Electrochemistry*, 2000, **68**, 942.

199. N. Hayazawa, Y. Inouye, Z. Sekkat and S. Kawata, *Opt. Commun.*, 2000, **183**, 333.
200. N. Hayazawa, Y. Inouye, Z. Sekkat and S. Kawata, *Chem. Phys. Lett.*, 2001, **335**, 369.
201. L. T. Nieman, G. M. Krampert and R. E. Martinez, *Rev. Sci. Instrum.*, 2001, **72**, 1691.
202. B. Pettinger, G. Picardi, R. Schuster and G. Ertl, *Single Mol.*, 2002, **5**, 285.
203. R. F. Aroca, P. J. G. Goulet, D. S. dos Santos, Jr., R. A. Alvarez-Puebla and O. N. Oliveira, Jr., *Anal. Chem.*, 2005, **77**, 378.
204. H. Yu, J. Zhang, H. Zhang and Z. Liu, *Langmuir*, 1999, **15**, 16.
205. Y. Wang, H. Chen, S. Dong and E. Wang, *J. Chem. Phys.*, 2006, **124**, 074709.
206. D. Buchel, C. Mihalcea, T. Fukaya, N. Atoda, J. Tominaga, T. Kikukawa and H. Fuji, *Appl. Phys. Lett.*, 2001, **79**, 620.
207. L. Liu and L. P. Lee, *Appl. Phys. Lett.*, 2005, **87**, 074101..
208. T. Park, S. Lee, G. H. Seong, J. Choo, E. Lee, Y. S. Kim, W. H. Ji, S. Y. Hwang, D. Gweon and S. Lee, *Lab Chip*, 2005, **5**, 437.
209. P. Etchegoin, R. C. Maher, L. F. Cohen, H. Hartigan, R. J. C. Brown, M. J. T. Milton and J. C. Gallop, *Chem. Phys. Lett.*, 2003, **375**, 84.
210. M. Fleischmann, P. J. Hendra and A. J. McQuillan, *Chem. Phys. Lett.*, 1974, **26**, 163.
211. [http://en.wikipedia.org/wiki/Alzheimer's\\_disease](http://en.wikipedia.org/wiki/Alzheimer's_disease)

212. M. Hashimoto, E. Rockenstein, L. Crews and E. Masliah, *Neuromolecular Med.*, 2003, **4**, 21.
213. I. Chou, M. Benford, H. T. Beier, G. L. Coté, M. Wang, N. Jing, J. Kameoka, T. A. Good, *Nano Lett.*, 2008, **8**, 1729.
214. K. Takano, S. Endo, A. Mukaiyama, H. Chon, H. Matsumura, Y. Koga and S. Kanaya, *FEBS J.*, 2006, **273**, 150.
215. P. T. Lansbury, *Neuron* 1997, **19**, 1151.
216. M. D. Kirkitadze, M. M. Condrón and D. B. Teplow, *J. Mol. Biol.* 2001, **312**, 1103.
217. T. Miura and G. J. Thomas, *Subcell. Biochem.*, 1995, **24**, 55.
218. T. Miura, K. Suzuki, N. Kohata and H. Takeuchi, *Biochemistry*, 2000, **39**, 7024.
219. E. Podstawka, Y. Ozaki and L. M. Proniewicz, *Appl. Spectroscopy*, 2004, **58**, 1147.
220. S. Stewart S. and P. M. Fredericks, *Spectrochimica. Acta. Part A*, 1999, **55**, 1615.
221. A. T. Tu, *Raman Spectroscopy in Biology*, John Wiley & Sons Inc, New York, USA, 1982.
222. N. T. Yu, C. S. Liu and D. C. O'Shea, *J. Mol. Biol.*, 1972, **70**, 117.
223. G. Shanmugam and P. L. Polavarapu, *Biophys. Chem.*, 2004, **111**, 73.
224. R. Wetzell, M. Becker, J. Behlke, H. Billwitz, S. Böhm, B. Ebert, H. Hamann, J. Krumbiegel and G. Lassmann, *Eur. J. Biochem.*, 1980, **104**, 469.
225. C. Jiang and J. Y. Chang, *FEBS Lett*, 2005, **579**, 3927.

226. J. L. Lippert, D. Tyminski and P. J. Desmuelles, *J. Am. Chem. Soc.*, 1976, **98**, 7075.
227. H. Zhao, B. Yuan and X. Dou, *J. Opt. A: Pure Appl. Opt.*, 2004, **6**, 900.
228. M. Benford, M. Wang, J. Kameoka and G. L. Cote, *Proc. SPIE*, 2009, **7192**, 719203.

## APPENDIX A

## Processing Parameters in a Successful Scanning Coaxial Electrospinning Process

Wall Material	A mixture of spin-on glass (SOG) intermediate coating IC1-200 solution and polyvinylpyrrolidone (PVP) Typical PVP concentration: 5%wt~8%wt Typical flow rate: 10ul/min	
Core Material	Motor oil Typical flow rate: 2ul/min	
Needle Size	Large needle: I.D. 1.07 mm, O.D. 1.47 mm. Small needle: I.D. 0.11 mm, O.D. 0.21 mm.	
External Electric Field	525V/cm	
Speed of rotating counter electrode	660~850 cm/s	
Target Substrate	Silicon wafer	
Calcination Temperature	850°C for 5 hours	

Constant Processing Parameters	PVP concentration: 5% Flow rate of SOG/PVP: 10 $\mu$ l/min Averaged applied electric field: 525V/cm	
Motor Oil Flow Rate	2 $\mu$ l/min	6 $\mu$ l/min
I.D of Resultant Nanochannels	29.8nm	39.25nm

## APPENDIX B

## Detailed Process Flow for Nanochannel Device for SERS

Substrate: Fused silica wafer, double sized polished, 500  $\mu\text{m}$  thick

Finished at Cornell Nanofabrication Facility

## First Level (Alignment Marker)

1. Spin coat P-20 primer and S1818 at 4000 rpm (ramp 2000 rpm/sec) for 30 sec
2. Softbake on a hotplate at 115°C for 1 min
3. Pattern first level (alignment marker) using contact lithography (EV 620, soft contact, exposure: 6 sec)
4. MIF 300 develop for 1min
5. Hardbake on a hotplate at 115°C for 1 min
6. Descum (Branson Barrel Etcher, room temperature, 4 min)
7. Etch alignment markers
  - (a) Oxford 80 oxygen plasma pre-clean (empty chamber) for 15 min
  - (b) Load wafer in Oxford 80, etch the alignment marker ( $\text{CHF}_3/\text{O}_2$ , 1 hr)
  - (c) Remove photoresist (Oxford 80,  $\text{O}_2$  plasma, 15 min)
8. Measured the depth of alignment marker to be  $\sim 1.2 \mu\text{m}$  (P10)
9. Remove photoresist residue on edge in resist strip hot bath for 30 min

## Second Level (Shallow Nanochannel)

10. Spin coat P-20 primer and S1813 at 4000 rpm (ramp 2000 rpm/sec) for 30 sec



11. Softbake on a hotplate at 115°C for 1 min
12. Aligned second level shallow channel with the first level alignment marker and patterned the shallow channel using contact lithography (EV 620, soft contact, exposure: 4 sec)
13. MIF 300 develop for 1min
14. Hardbake on a hotplate at 115°C for 1 min
15. Descum (Branson Barrel Etcher, room temperature, 4 min)
16. Etch shallow nanochannel
  - (a) Oxford 80 oxygen plasma pre-clean for 15 min and CF<sub>4</sub> seasoning for 5 min (empty chamber)
  - (b) Load wafer in Oxford 80, etch the shallow nanochannel (CF<sub>4</sub>, 2.5 min)
  - (c) Remove photoresist (Oxford 80, oxygen plasma, 15 min)
17. Measured the depth of shallow nanochannel to be ~50nm (P10)
18. Remove photoresist residue on edge in resist strip hot bath for 30 min
19. Deposit Amorphous silicon layer on the wafer (GSI PECVD)
  - a) Clean recipe for 10 min
  - b) Pre-deposit A-Si for 3 min (dummy wafer)
  - c) Deposit 3 min at 400°C (~250nm)

### Third Level (Deep Microchannel)

20. Spin coat P-20 primer and S1818 at 4000 rpm (ramp 2000 rpm/sec) for 30 sec
21. Softbake on a hotplate at 115°C for 1 min

22. Aligned third level deep channel with the first level alignment marker and patterned the deep channel using contact lithography (EV 620, soft contact, exposure: 6 sec)
23. MIF 300 develop for 1min
24. Hardbake on a hotplate at 115°C for 1 min
25. Descum (Branson Barrel Etcher, room temperature, 4 min)
26. Etch A-Si in deep channel area
  - (a) Oxford 80 oxygen plasma pre-clean for 15 min and CF<sub>4</sub> seasoning for 5 min (empty chamber)
  - (b) Load wafer in Oxford 80, etch the A-Si in patterned deep channel area (CF<sub>4</sub>, etch time: 10 min)
27. Etch the deep channel using wet etching (HF49%, etch time: 1.5 min)
28. Rinse with DI water three times and blow dry
29. Measured the depth of deep channel to be ~2 um (P10)
30. Remove photoresist in resist strip hot bath for 30 min and blow dry
31. Remove A-Si layer
  - (a) Oxford 80 oxygen plasma pre-clean for 15 min
  - (b) Remove A-Si layer (Oxford 80, SF<sub>6</sub>/O<sub>2</sub>, 3 min)

#### Creating of Inlet/Outlet Holes

32. Spin coat P-20 and FSC-M at 3000 rpm (ramp 1000rpm/sec) for 1 min
33. Air oven bake at 90°C for 3 hr
34. Mark holes on the wafer and sand blaster through

35. Remove protective photoresist in resist strip hot bath for 30 min
36. Put wafers (processed and intact) in nanostrip (overnight), rinse three times and blow dry
37. Cling a processed wafer with an intact wafers in DI water, take out and dry naturally in air
38. Put the pre-bonded wafer in furnace and heat at 1050°C for 7 hours (timer set to 7 hrs)

#### Attach Plastic Reservoirs

39. Attached plastic reservoirs around the inlet/outlet holes using 5-min epoxy

## VITA

Name: Miao Wang

Address: Department of Electrical Engineering, Texas A&M University  
College Station, TX 77843-3128

Email Address: miao@tamu.edu

Education: B. En., Electronic Engineering & Information Science,  
University of Science & Technology of China, July 2003  
Ph.D., Electrical Engineering  
Texas A&M University, August 2009

## Selected Publications:

1. M. Benford, G. L. Coté, J. Kameoka and M. Wang, book chapter in “Handbooks of Optofluidics”, edited by A. R. Hawkins, H. Schmidt, Taylor & Francis Books, Inc. 2010
2. M. Wang and J. Kameoka, Chapter 5 in “*Nanofluidics: Nanoscience and Nanotechnology*”, edited by Joshua B. Edel and Andrew J. deMello, Royal Society of Chemistry, UK, 2009
3. M. Wang, M. Benford, N. Jing, G. Coté and J. Kameoka, “Optofluidic device for ultra-sensitive detection of protein using surface-enhanced Raman Spectroscopy”, *Microfluidics & Nanofluidics*, Vol. 6, 411(2009)
4. I. Chou, M. Benford, H. T. Beier, G. L. Cote, M. Wang, N. Jing, J. Kameoka, T. A. Good, “Nanofluidic Biosensing for  $\beta$ -Amyloid Detection Using Surface Enhanced Raman Spectroscopy”, *Nano Letter*, Vol. 8, 1729 (2008), *Highlighted by Nature* Vol. 453, 701 (5 June 2008)
5. M. Wang, N. Jing, J. Kameoka, I. Chou and G. Coté, “Optofluidic device for surface enhanced Raman spectroscopy”, *Lab on a Chip*, Vol. 7, 630 (2007)
6. M. Wang, N. Jing, C. Su, C. Chou, M. Hung, K. Chang, J. Kameoka, “Electrospinning of silica nanochannels for single molecule detection”, *Applied Physics Letter*, Vol. 88, 033106 (2006)
7. N. Jing, M. Wang and J. Kameoka, “Fabrication of Ultrathin ZrO<sub>2</sub> Nanofibers by Electrospinning”, *Journal of Photopolymer Science and Technology*, Vol. 18, 503 (2005)